DOE/ET/20562-4

THIN-FILM POLYCRYSTALLINE SILICON SOLAR CELLS

Final Report for September 11, 1978—September 10, 1979

By
B. W. Faughnan

November 1979

Work Performed Under Contract No. AC03-78ET20562

RCA Laboratories
Princeton, New Jersey

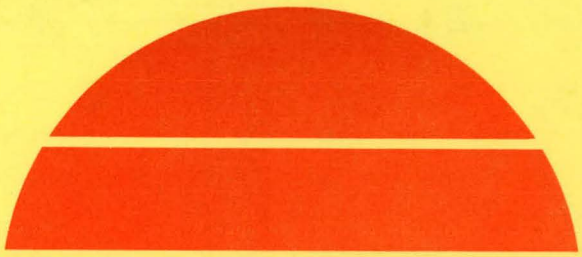

U.S. Department of Energy

Solar Energy

2205

DISCLAIMER

DISCLAIMER

Available from the National Technical Information Service, U. S. Department of Commerce, Springfield, Virginia 22161.

Price: Paper Copy $7.00
Microfiche $3.50

DOE/ET/20562-4
Distribution Category UC-63

THIN-FILM POLYCRYSTALLINE SILICON SOLAR CELLS

B. W. Faughnan
RCA Laboratories
Princeton, New Jersey 08540

NOVEMBER 1979

FINAL REPORT
For the Period 11 September 1978 to 10 September 1979

Contract No. AC-03-78ET-20562 (Formerly ET-78-C-03-1876)

Prepared for
Department of Energy
San Francisco Operations
1333 Broadway
Oakland, California 94612

THIS PAGE

WAS INTENTIONALLY

LEFT BLANK

PREFACE

This Final Report, prepared by RCA Laboratories, Princeton, NJ 08540, describes work performed from 11 September 1978 to 10 September 1979 in the Energy Systems Research Laboratory, B. F Williams, Director. The Project Scientist is B. W. Faughnan and the Project Supervisor is A. H. Firester, Head, Process and Applications. Others who participated in this research and the preparation of this report are J. Blanc, W. Phillips, and D. Redfield.

This report number is PRRL-79-CR-48.

THIS PAGE

WAS INTENTIONALLY

LEFT BLANK

ABSTRACT

The effect of grain boundaries on the performance of solar cells fabricated on Wacker Silso polycrystalline silicon substrates has been studied. Efficiencies of 8% (no AR coating) were obtained (11.2% with AR coating). This is 20% lower than the efficiency obtained for identically fabricated single-crystal cells. This reduction can be accounted for as follows: 4% reduction in V_{oc} due to grain boundaries, 8% reduction in J_{sc} due to grain boundaries, and 8% reduction in J_{sc} due to a lower minority carrier diffusion length inside the grains.

Quantum efficiency measurements were made with a 150-μm-diameter light spot inside grains and across grain boundaries, permitting a determination of L_n inside a grain (L_n = 75 μm for Wacker Silso). Laser scans were obtained at λ = 0.633 μm and at λ = 1.15 μm. Some grain boundaries are shown to be electrically inactive. Active grain boundaries were also observed by a novel liquid-crystal technique. Deep traps were studied by DLTS. The crystallographic orientation of individual grains was measured by an SEM technique called electron channeling patterns. Two silicon bicrystals were grown with well defined grain boundaries [(111) growth directions, 30° and 5° misorientation between the (110) directions].

THIS PAGE

WAS INTENTIONALLY

LEFT BLANK

TABLE OF CONTENTS

TABLE OF CONTENTS (Continued)

LIST OF ILLUSTRATIONS

LIST OF ILLUSTRATIONS (Continued)

LIST OF TABLES

SECTION I

SUMMARY

The effects of grain boundaries on the performance of solar cells fabricated on polycrystalline silicon substrates have been studied by a variety of techniques. Solar cells were fabricated directly on Wacker* "Silso" polycrystalline silicon wafers which were used throughout this study as a prototype material.

Equally efficient solar cells could be obtained with junctions formed by diffusion or by ion implantation followed by a suitable anneal cycle. The best efficiency obtained was 8.2% for a polycrystalline cell and 10.0% for a single-crystal control cell, both without antireflection (AR) coatings. With AR coatings these numbers would be approximately 11.5% and 14%, respectively. Thus the efficiency of solar cells made on Wacker polycrystalline substrates is reduced approximately 20% from their single-crystal counterparts. We show from detailed quantum efficiency measurements that approximately half of this reduction is due to grain boundary effects and half is due to reduced minority carrier diffusion length in the polycrystalline material.

A number of experimental techniques are developed for studying grain boundary effects more directly. The effective value of the base diffusion length is determined from measured quantum efficiency data by curve fitting to theoretical curves for a simple model diode. By using a small-diameter light spot focused inside a grain, true bulk diffusion lengths can be obtained. We find $L_n \tilde{>} 75$ μm for Wacker material inside a grain, but this value is reduced to 35 to 45 μm when an average value including many grain boundaries is measured. Laser scans showing the photoresponse of grain boundaries over large areas of the solar cell are obtained. Scans at $\lambda = 0.633$ μm show that some grain boundaries have no photoresponse (electrically inactive) while others may have a variable photoresponse along the boundary. Laser line scans at $\lambda = 1.15$ μm are ideal for detailed grain boundary study since electron-hole pairs are created uniformly with depth in the base region of the diode. We

*Wacker Chemical Corp., Richardson, TX.

find the full width at half maximum in the photoresponse of an active grain boundary is 200 to 300 μm at this wavelength.

We have begun the study of deep-trap states at grain boundaries by deep-level transient spectroscopy (DLTS). While no definitive results have been obtained so far, many of the considerable problems encountered using this technique have been addressed, and new results are hoped for in the coming year. A novel technique was developed for observing active grain boundaries by applying a thin film of liquid crystal on top of the polycrystalline substrate. When an electric field is applied to the liquid crystal, some of the grain boundaries light up when viewed through crossed polarizers.

The scanning electron microscope (SEM) technique of electron channeling patterns (ECP) is used to determine the crystallographic orientation of individual grains. This presents the possibility of correlating the misorientation between grains with the degree of electrical activity of the grain boundary. The phosphorus concentration profile in diffused samples was measured by secondary ion-mass spectroscopy (SIMS), yielding the unexpected result that phosphosus diffusion is reduced in regions near grain boundaries (but not necessarily down the grain boundary itself).

Two silicon bicrystals were grown in order to study well-defined grain boundaries. In the first bicrystal the growth direction for both grains was (111), with a 30° misorientation between the (110) directions of the two grains. A dip in photoresponse due to this grain boundary was observed in a laser scan across a solar cell fabricated on a wafer cut from this bicrystal.

SECTION II

INTRODUCTION

Developing high-efficiency solar cells in polycrystalline silicon requires a better understanding of the chemical and defect structure of the intergrain boundaries and their effect on the electrical properties of p-n junctions than is available at this time. Our goal is to obtain an understanding of the electrical properties of grain boundaries as a function of the chemical and defect structure. Our approach is to prepare solar-cell structures on Wacker Silso polycrystalline substrates and then to study the optical and electrical properties of these grain boundaries and estimate their effect on the degradation of solar-cell properties. We hope to isolate and identify grain boundaries showing the most degraded photoresponse.

SECTION III

PREPARATION AND AM-1 MEASUREMENT OF SOLAR CELLS

A. PREPARATION OF SOLAR-CELL STRUCTURES

1. Polycrystalline Material

The Wacker Silso material used for the fabrication of our solar cells was obtained from Wacker Chemical Corp. in the form of 4x4-in. wafers. The silicon is cast into a 4x4-in. ingot, and the wafers are sliced from this ingot. The material is polycrystalline with some large single-crystal grains (3 to 6 mm) in the center region and long, narrow (10x1 mm) grains near the edge which are oriented perpendicular to the edges. The average grain size is perhaps 1 mm in linear dimension although no actual averaging was carried out. A photograph of a 4x4-in. wafer clearly showing the grain structure is shown in Fig. 1.

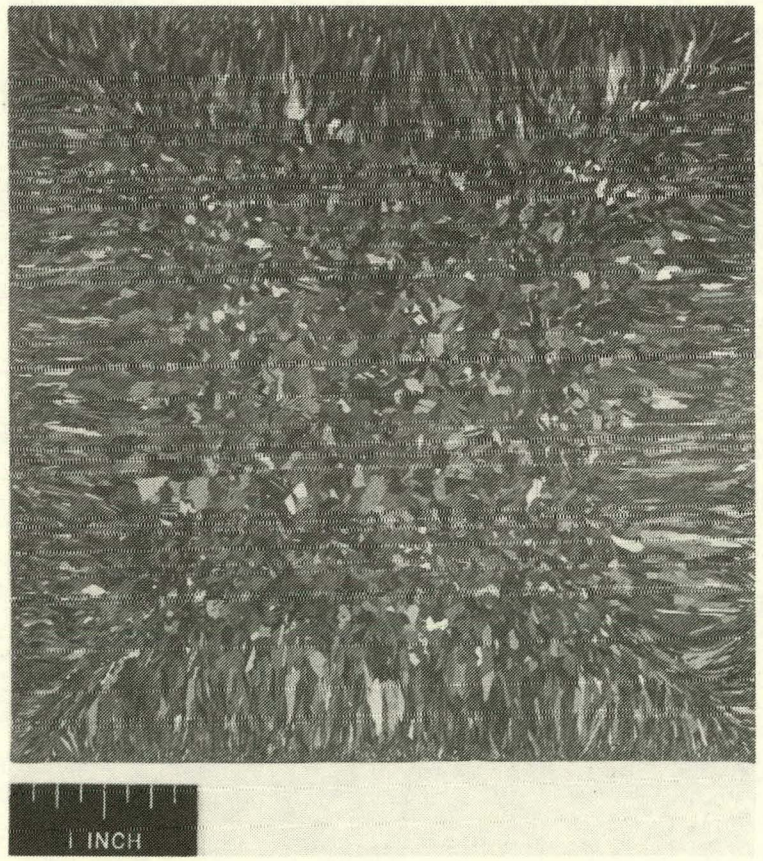

Figure 1. Photograph of a Wacker Silso 4x4-in. wafer showing grain structure.

2. Junction Formation

The Wacker substrates are p-type, 6-Ω-cm nominal resistivity. Junctions were formed in the substrates by creating an n-type phosphorus skin layer in one of two ways; diffusion or ion implantation followed by suitable annealing steps. The two methods were used because they might have quite different effects on the possible passivation of grain boundaries by phosphorus diffusion down these boundaries.

The diffused junctions were formed by diffusion from a $POCl_3$ gas at temperatures in the 850 to 900°C range. A typical diffusion schedule is 5-min soak, N_2 gas; 20-min $POCl_3$ gas; 25-min soak, N_2 gas, all at 875°C. The second step produces a glassy phosphorus-containing deposit on the surface of the wafer, while the third step is responsible for the diffusion of phosphorus into the wafer. A junction depth between 0.3 and 0.5 μm is usually obtained. A p^+ region was also formed on the backside of each wafer by boron diffusion. This ensured good ohmic contact when the metallization was applied.

The ion-implanted wafers were processed as follows:

Dose:	2×10^{15} phosphorus atoms/cm^2, 5 keV	Front side (junction)
	5×10^{15} boron atoms/cm^2, 25 keV (junction depth ∿ 0.3 μm)	Back side (p^+ region)
Anneal:	3 steps (1) 550°C, 2 h, N_2 gas	
	(2) 850°C, 15 min, N_2 gas	
	(3) 550°C, 2 h, N_2 gas	

At 5 keV the penetration depth of phosphorus atoms is only 400 to 500 Å. Therefore, the annealing step is responsible both for removing the radiation damage and diffusing the phosphorus in to a depth of 0.3 to 0.5 μm. It is also important to carry out these steps in such a way that the minority carrier base diffusion length is not degraded.

After junction formation by either technique, the sheet resistance is measured to check that a proper junction has been formed. The actual junction depth is directly measured by two techniques, spreading resistance measurement and beveling and staining. Figure 2 shows the results of a spreading resistance measurement. This measurement also gives the concentration profile of electrically active dopant atoms. The staining technique is illustrated in Fig. 3 for the same wafer, where a junction depth of 0.44 μm is obtained, in agreement with the spreading resistance measurement.

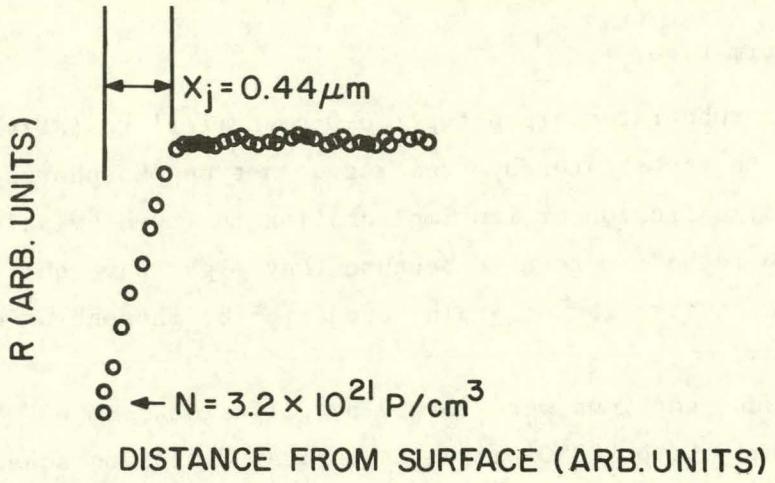

Figure 2. Spreading resistance measurement of the junction in Wacker cell 473.

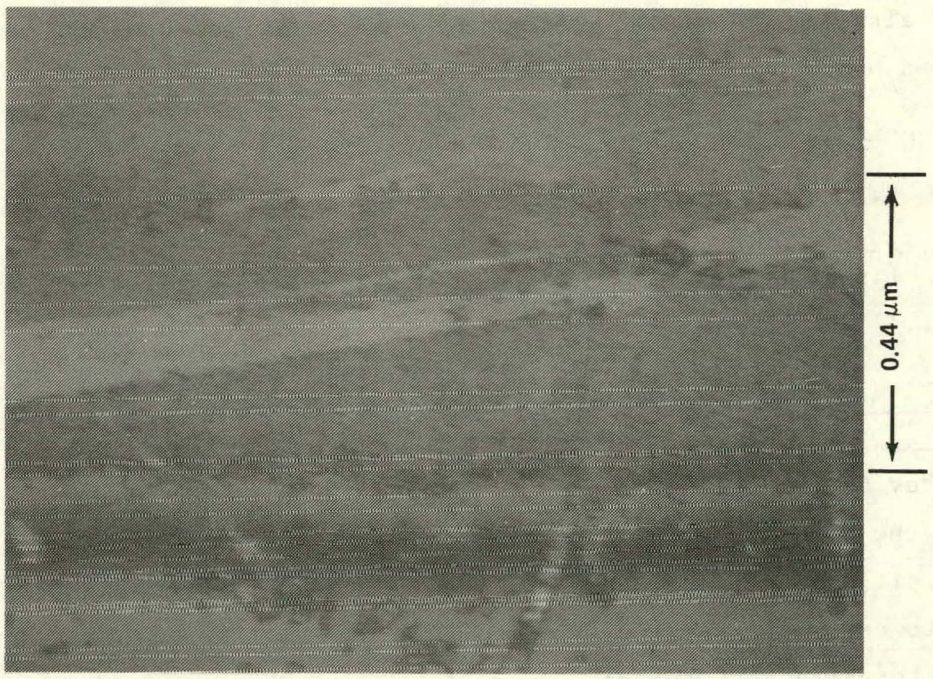

Figure 3. Measurement of junction depth by staining in cell 473.

3. Device Fabrication

Prior to junction formation the 10x10-cm Wacker substrates are cut into four 5x5-cm wafers. One mil of material is etched from each side to remove saw damage. For some cells, the junction is formed directly on the etched surface while for other cells the surface is first given a chemical-mechanical polish.

Metallization is applied by evaporation of Ti/Ag. The front fingers are defined photolithographically and the active area of 4.5 cm^2 is mesa etched. In addition to the 4.5-cm^2-area solar cell, two smaller solar cells and a series of diode dots are formed on each wafer for increased measurement flexibility. Some cells had an AR coating applied, but usually this is not done because the interpretation of measurements is facilitated without it.

B. MEASUREMENT OF SOLAR-CELL PARAMETERS

1. Initial Set of Diffused- and Ion-Implanted Junction Solar Cells

Approximately 100 solar cells were fabricated during the course of this contract; however, detailed measurements were taken only on 50 of them. Of the approximately 50 cells for which we do not present data, 25 were completed, but found to be defective for one reason or another. The other 25 cells are either completed and not characterized or are not completed. These cells will be used in the coming year.

The AM-1 parameters and the junction depth and sheet resistance data (when available) for the 50 solar cells studied are presented in this section in a series of tables. This data will be referred to throughout this report where appropriate.

AM-1 measurements are made with ELH lamp simulation, 100-mW/cm^2 incident light. Single-crystal control cells are included in all cases for comparison. The initial set of eight diffused cells is shown in Table 1; the initial set of ion-implanted cells is shown in Table 2. The numbers listed under the column heading L_n (minority carrier base diffusion length) are derived from quantum efficiency curves and will be discussed in Section IV.

Several conclusions can be drawn from the data of Tables 1 and 2. The average efficiencies for single-crystal controls, Wacker polished (surface), and Wacker etched (surface), with and without AR coatings, for diffused-junction cells 401-408 are shown in Table 3. For polished surfaces, the efficiency (and J_{sc}) increased by a factor of 1.4 with AR coating. Since all subsequent cells are measured without AR coating, this factor should be kept in mind. On the other hand the Wacker etched (surface) cells have a higher average efficiency than the Wacker polished cells without AR coating, but a lower average efficiency when AR coating is applied. This is because etched cells have a rough, textured surface (see Section VI.A) which reduces the amount of reflected

TABLE 1. MEASURED SOLAR-CELL PARAMETERS, DIFFUSED JUNCTIONS

Diffusion conditions: 20-min phosphorus deposition, 25-min drive-in; T = 875°C

AR Coating

Sample No. and Type*	Sheet ρ (Ω/□)	L_n (μm)	J_{sc} (mA/cm^2)	V_{oc} (mV)	FF -	η (%)
401C	(See below)		30.6	567	0.73	12.7
402P			26.7	541	0.75	10.8
403P			27.2	535	0.74	11.1
404E			25.4	525	0.73	9.7
405C			31.4	548	0.74	12.7
406E			26.7	529	0.73	10.3
407P			27.5	539	0.71	10.5
408E			24.5	520	0.70	8.9

No AR Coating

401C	37	250	22.7	558	0.71	9.0
402P	34	30	19.8	535	0.71	7.5
403P	68	50	19.5	530	0.71	7.4
404E	35	60	22.7	523	0.75	8.8
405C	47	200	22.0	543	0.79	9.4
406E	47	70	20.4	526	0.75	8.1
407P	43	45	19.2	535	0.61	6.3
408E	116	45	20.0	520	0.76	7.9

*C - control sample, single-crystal wafer, polished surface
P - Wacker Silso polycrystalline wafer, polished surface
E - Wacker Silso polycrystalline wafer, etched surface

(AM-1 parameters, 100 mW/cm^2 incident light intensity, ELH lamp simulation)

TABLE 2. MEASURED SOLAR-CELL PARAMETERS, ION-IMPLANTED JUNCTIONS

Implant conditions: dose: 2×10^{15} phosphorus atoms/cm^2; anneal: 550°C, 2 h, 850°C, 15 min, 550°C, 2 h.

No AR Coating

Sample No. and Type	Sheet ρ (Ω/□)	L_n (μm)	J_{sc} (mA/cm^2)	V_{oc} (mV)	FF -	η (%)
409C	99	80	21.9	521	0.75	8.6
410E	74	3 (8)	18.9	508	0.70	6.7
411E	82	4 (14)	18.3	487	0.68	6.0
412P	85	4 (8)	17.3	480	0.66	5.5
413C	106	80	21.5	518	0.76	8.5
414P	90	6 (20)	19.1	513	0.72	7.0
415P	74	2 (8)	17.3	460	0.66	5.3
416E	88	6 (14)	19.2	492	0.70	6.6

TABLE 3. COMPARISON OF AVERAGE EFFICIENCIES OF DIFFUSED CELLS, WITH AND WITHOUT AR COATING

Type of Cell	η (%) No AR -	η (%) AR -	% Increase
Single-Crystal Control	9.2	12.7	1.38
Wacker Polished	7.4	10.8	1.47
Wacker Etched	8.3	9.6	1.17

light. However, this surface roughness also reduces the effectiveness of the AR coating when applied. For this reason all detailed optical measurements in this report will be done on polished surfaces where the surface reflectivity of light can be reasonably estimated or measured.

The average efficiency of the Wacker polished-surface, diffused-junction cells is reduced by about 20% from the single-crystal controls which received the same treatment. This reduction is typical of all the solar cells measured in this report. The ion-implanted junction Wacker solar cells have an average efficiency 20% below the diffused-junction Wacker cells. However, subsequent ion-implanted cells have improved efficiency so that this result does not appear to be fundamental. We note that the ion-implanted junctions were annealed at 850°C for 15 min, whereas the diffused-junction cells were treated at 875°C for 25 min. We learned that the lower temperature and time is insufficient to produce a good junction in Wacker material. Evidence of this is seen in the higher values of sheet ρ observed in the ion-implanted junctions compared with the diffused junctions.

2. Edge versus Center of Wacker Wafers

An examination of a typical Wacker substrate (see Fig. 1) shows that the first 1 to 2 cm from the edge has a different crystallographic grain structure from the central region. This presumably is related to the way the ingot is cooled during growth. The question arises whether solar cells made from the edge region have different properties from those made using the central region. The series 434-439 was designed to answer this question. These six cells include two single-crystal controls, two solar cells made from the center region (only one 2x2-cm solar cell per 10x10-cm wafer), and two cells made from edge cuts. Actually, for the edge cuts, the 10x10-cm wafer was quartered, and the 2x2-cm solar cell was centered on the resulting 5x5-cm wafer. Therefore, the active cell is only partially made up of edge-region material. The results of the test are shown in Table 4. The difference between edge and center cut is not great, although η_{ave} is 8% higher for the center cut compared with the edge cut. Since the center cut is very wasteful of material, we shall make all of our future solar cells by first quartering the 10x10-cm wafer unless otherwise specified.

3. Diffusion Drive-in Temperature

Nine diffused-junction solar cells were prepared at three different diffusion temperatures, 900, 875, and 850°C. In each case the $POCl_3$ gas flowed for 15 min and was followed by a 25-min drive-in at the same temperature. Three

cells were prepared at each temperature: single-crystal control, Wacker etched surface, and Wacker polished surface. The I-V parameters of cells are given in Table 5.

TABLE 4. SOLAR-CELL PARAMETERS AS A FUNCTION OF CENTER VERSUS EDGE CUT ON WACKER 10x10-cm WAFERS

Diffusion conditions: 20-min phosphorus deposition, 25-min drive-in; T = 875°C

Sample No.	Type	Sheet ρ (Ω/□)	J_{sc} (mA/cm^2)	V_{oc} (mV)	FF	η(no AR) (%)	η(ave) (%)
434C	Control	41.1	21.6	532	0.78	8.9	8.5
435C	Control	56.8	20.8	535	0.72	8.1	
436	Edge	70.9	19.1	522	0.74	7.4	6.9
437	Edge	57.3	18.8	518	0.66	6.4	
438	Center	48.2	19.4	530	0.75	7.7	7.5
439	Center	54.0	19.2	525	0.73	7.4	

TABLE 5. SOLAR-CELL PARAMETERS AS A FUNCTION OF JUNCTION DIFFUSION TEMPERATURE

Diffusion conditions: 15-min phosphorus deposition, 25-min drive-in

Sample No. & Type	Diff Temp (°C)	Sheet ρ (Ω/□)	J_{sc} (mA/cm^2)	V_{oc} (mV)	FF	η (no AR) (%)
440C	900	18.0	21.5	559	0.77	9.2
441E	900	20.1	20.3	532	0.76	8.3
442P	900	19.1	20.0	537	0.76	8.1
443C	875	51.6	21.7	546	0.77	9.1
444E	875	44.4	19.4	528	0.76	8.0
445P	875	37.7	19.1	515	0.75	7.4
446C	850	149	21.9	530	0.76	8.8
447E	850	212	5.2	146	0.48	0.4
448P	850	220	17.2	348	0.43	2.6

The cells whose junctions were diffused at 875°C have solar-cell parameters very similar to cells 401 to 408 [1] whose junctions were formed at the same

1. H. J. Hovel, in Semiconductors and Semimetals, Vol. 11, R. K. Willardson and A. C. Beer, eds. (Academic Press, New York, 1975), ch. 2, "Solar Cells."

temperature. The 900°C junctions were not very different. However, there is a big difference between the control and the Wacker cells for the 850°C run. The control cell follows the same general pattern, i.e., J_{sc} rises as diffusion temperature drops whereas V_{oc} varies in the opposite way. The net result is that the efficiency varies only slightly from 850 to 900°C. However, the Wacker cells made at 850°C are very poor. There was some indication from earlier work done at RCA on Wacker substrates that diffusion is not very effective at 850°C or below.

4. Recent Diffused- and Ion-Implanted Junction Solar Cells

The three last series of solar cells are summarized in Tables 6, 7, and 8. Two sets have ion-implanted junctions and one set has diffused junctions.

TABLE 6. SOLAR-CELL PARAMETERS FOR A SET OF ION-IMPLANTED JUNCTION CELLS

Implant conditions: dose: 2×10^{15} phosphorus atoms/cm^2; anneal: 550°C, 2 h, 875°C, 15-min, 550°C, 2 h.

Sample No.	Sheet ρ (Ω/□)	J_{sc} (mA/cm^2)	V_{oc} (mV)	FF	η(no AR) (%)
463C	131	20.3	512	0.77	8.2
464P	159	19.5	528	0.69	7.1
465E	114	19.9	520	0.67	6.6
466C	116	21.6	532	0.75	8.7
467P	123	19.0	523	0.70	7.0
468E	122	19.1	525	0.74	7.4

The first set of ion-implanted cells (Table 6), in which the high-temperature anneal is carried out at 875°C, shows much improved AM-1 parameters compared with the first set annealed at 850°C (Table 2). The average efficiency with no AR coating for Wacker polished surface cells increases from 5.6 to 7.1%. This is still below the average efficiency for the first set of diffused cells (Tables 1 and 2) which is 7.4% and the most recent set (Table 7) which is 7.9%. However, the average efficiency of the final set of ion-implanted cells (Table 8), in which the annealing temperature is increased to 900°C, has improved to 7.6%. This is better than all the diffused cells except the last set. This leads to the conclusion that diffused-junction cells and ion-implanted junction cells can be made with comparable AM-1 parameters, but the proper annealing conditions must be found.

TABLE 7. SOLAR-CELL PARAMETERS FOR A SET OF DIFFUSED-JUNCTION CELLS

Diffusion conditions: 20-min phosphorus deposition; 25-min drive-in for cells 472-74, 45-min drive-in for cells 475-78; T = 875°C

Sample No.	Sheet ρ (Ω/□)	x_j* (μm)	x_j† (μm)	J_{sc} (mA/cm^2)	V_{oc} (mV)	FF	η (%)
472	169	0.33	0.25	15.9	549	0.72	7.5
473	40	0.50	0.50	19.9	542	0.77	8.3
474	48	0.40	0.40	18.5	526	0.76	7.4
475	222	0.30	0.23	20	532	0.76	8.1
476	37	0.48	0.48	19.9	540	0.76	8.2
478C	32	0.60	0.53	23.2	562	0.77	10.0

*Obtained from spreading resistance measurements.
†Obtained from beveling and staining measurements.

All cells have polished surfaces.

TABLE 8. SOLAR-CELL PARAMETERS FOR A SET OF ION-IMPLANTED CELLS

Implant conditions: dose: 4×10^{15} phosphorus atoms/cm^2; anneal: 550°C, 2 h, 900°C, 15 min, 550°C, 2 h.

Sample No.	Sheet (Ω/□)	J_{sc} (mA/cm^2)	V_{oc} (mV)	FF -	η (No AR) (%)	η* (AR)
479C	62	22.7	553	0.75	9.4	13.2
480	64	19.4	528	0.76	7.8	10.9
481	61	19.9	520	0.74	7.7	10.8
482C	59	23.3	566	0.79	10.4	14.6
483	60	19.2	520	0.74	7.4	10.4
484	61	18.7	517	0.74	7.2	10.1
485C	61	25.0	563	0.77	10.8	15.1
488C	64	22.0	528	0.77	9.0	12.6

*Obtained from η(no AR) by multiplying by 1.4
All cells have polished surfaces.

5. Summary of AM-1 Measurements

Diffused-junction and ion-implanted junction solar cells can be made with comparable efficiency. A diffusion temperature between 875 and 900°C appears optimum for both types of junctions. This leads to junction depths in the 0.3- to 0.5-μm range. We were not able to make good solar cells on Wacker substrates at a diffusion temperature of 850°C, although good single-crystal

cells can be made at this temperature. We have some evidence, from direct measurement of the junction depth, that diffusion proceeds more slowly in the Wacker material compared with single-crystal silicon at 850°C and possibly at higher temperatures as well.

The best efficiency obtained for a Wacker cell (473) is 8.3% (no AR) compared with 10% for a single-crystal control (478) processed the same way (Table 7). For these two cells J_{sc} is reduced by 14%, V_{oc} by 4%, leading to a 18% reduction in efficiency for the Wacker polycrystalline solar cell.

The light I-V curves for a Wacker diffused cell, Wacker ion-implanted cell, and a single-crystal control cell are shown in Fig. 4.

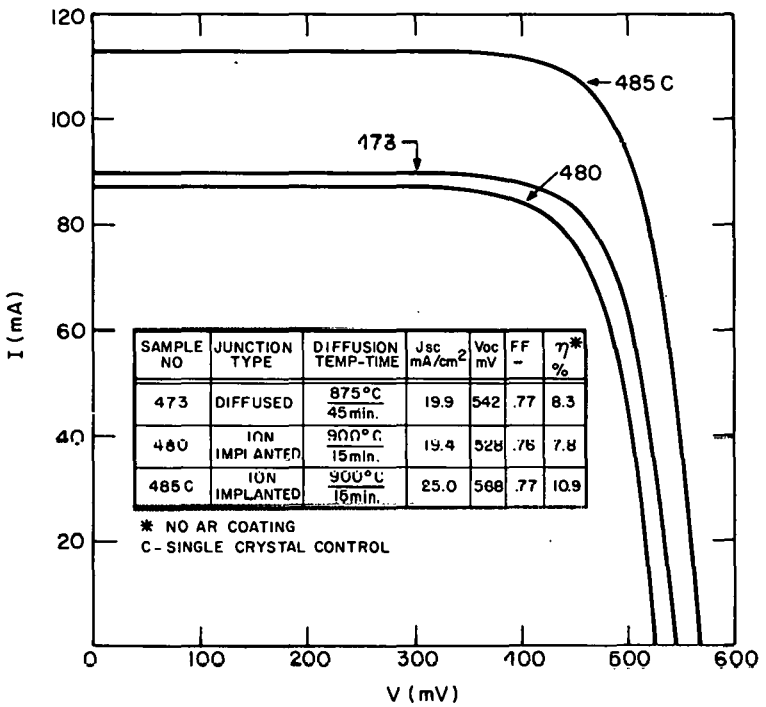

Figure 4. Light I-V curves for Wacker polycrystalline and single-crystal solar cells.

SECTION IV

ELECTRICAL AND OPTICAL MEASUREMENTS OF POLYCRYSTALLINE SILICON

A. QUANTUM EFFICIENCY AND BASE DIFFUSION LENGTHS

1. Modeling of Solar-Cell Quantum Efficiency

The quantum efficiency (or collection efficiency) of a solar cell can be easily derived on the basis of a simple one dimensional model. The details can be found in the book by Hovel [1]. The n and p regions of the diode are assumed to be uniform and homogeneous and can be described by constant minority carrier diffusion lengths L_p and L_n, respectively. As a result of this assumption there are no internal electric fields and the collection current is obtained by solving the diffusion equation in the skin and base regions. The boundary conditions at the front and back surfaces are expressed in terms of minority carrier surface recombination velocities S_p and S_n, respectively.

The seven parameters that enter the theory are:

(1) x_j = junction depth in microns. This can be measured directly by spreading resistance or by staining.

(2) W = depletion width in base region in microns. This will be on the order of 1 μm. In this region cell carriers are swept to the junction by the strong electric field that exists there. However, for all values of base diffusion length of interest in this report, W can be set equal to zero with negligible error.

(3) h is the total width of the diode in microns.

(4) L_p is the diffusion length for holes in the n-type skin region in microns.

(5) L_n is the diffusion length for electrons in the p-type region.

(6) S_p/D_p is the ratio of the front surface recombination velocity to diffusion constant for holes in $(\mu m)^{-1}$.

(7) S_n/D_n is the ratio of the back surface recombination velocity to diffusion constant for electrons in the base region.

If values for all seven parameters are known or assumed, then the quantum efficiency can be calculated and compared with experiment. We shall use this method to deduce the minority carrier diffusion length in the base.

The procedure is as follows. The first three parameters are known, i.e., x_j, W, and h. (Actually W is set equal to zero as discussed above.) Some combination of L_p and S_p/D_p is determined to give the best fit in the short wavelength portion of the spectrum. Once this is determined, the same values are used throughout all the curve fitting in this report since there should be no reason for them to vary. The value of L_n is varied until a good fit in the long wavelength part of the spectrum is obtained. A high value for the surface recombination velocity at the back surface is usually assumed, i.e., $S_p = 5 \times 10^4 cm^2/s$, $D_p = 1$, $S_p/D_p = 5 \times 10^4\ cm^{-1} = 5\ \mu m^{-1}$. If L_n is one half or less of h, then the quantum efficiency curve is affected very little by the value chosen for S_n. An approximation often used for an ohmic contact is $S_n = \infty$, while an approximation for a back surface field (p^+p layer) is $S_n = 0$. Fortunately the value of QE over the spectral range $0.60 < \lambda < 1.0\ \mu m$ is most sensitive to the value chosen for L_n, independent of the values chosen for the other parameters, so that a good estimate of L_n can be obtained by this technique. In addition to the seven parameters listed above, the absorption of light in silicon as a function of wavelength must be put into the theory.

The response of the base region alone for a range of base diffusion lengths is shown in Fig. 5.

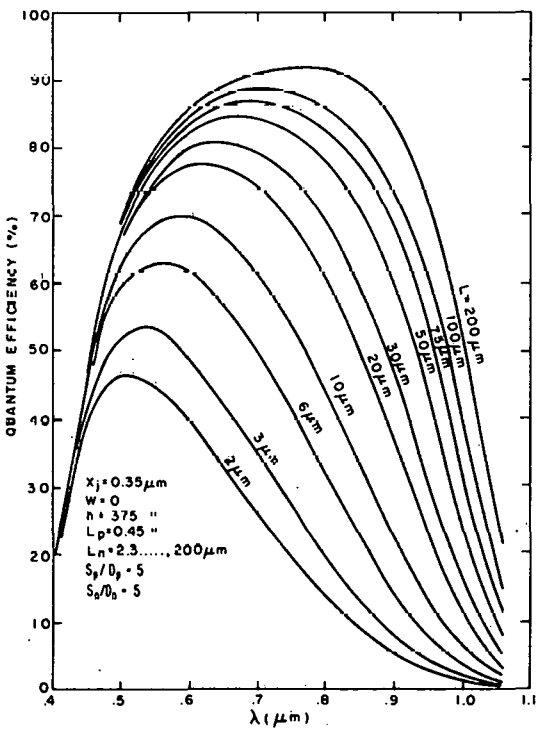

Figure 5. Theoretical base response of a solar cell for a variety of base diffusion lengths.

The skin response for different values of L_p and S_p/D_p is shown in Fig. 6.

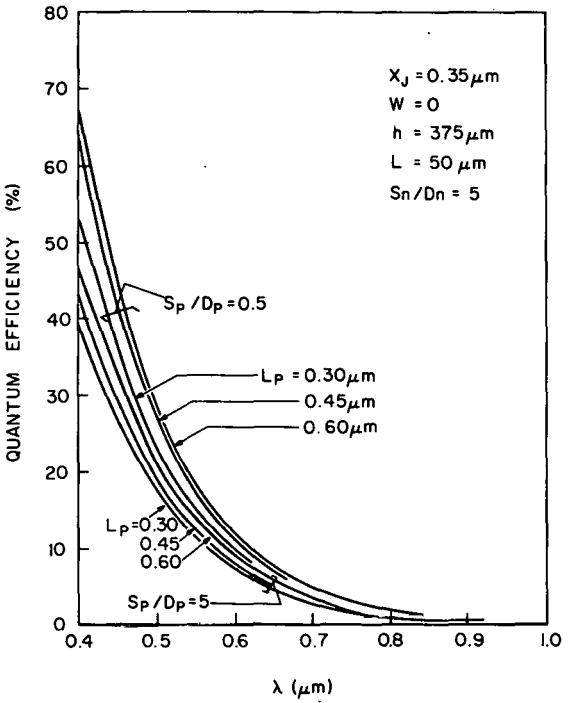

Figure 6. Theoretical skin response of a solar cell for different values of L_p and S_p/D_p.

The effect of different values of x_j and S_p/D_p on the total quantum efficiency is shown in Fig. 7. The spectral response beyond $\lambda = 0.8$ μm is determined solely by the base diffusion length L_n.

2. Measurement of QE and Determination of Base Diffusion Lengths

The quantum efficiency measurements discussed in this section make use of an apparatus which we set up before the start of this contract. The spectral range between 0.4 μm and 1.1 μm is covered by 12 narrow-band (50-Å width) interference filters. The light from a tungsten source is chopped and detected by a PAR* phase sensitive detector. Suitable optics are provided for collecting, collimating, and focusing the beam. The light beam is in the form of a 1x8-mm^2 slit which is focused on the solar cell under test between the metal fingers. A beam splitter directs a known fraction of light to a silicon photodetector. The photoresponse of this detector has been calibrated by means of an NBS standard

*Princeton Applied Research Corp., Princeton, NJ.

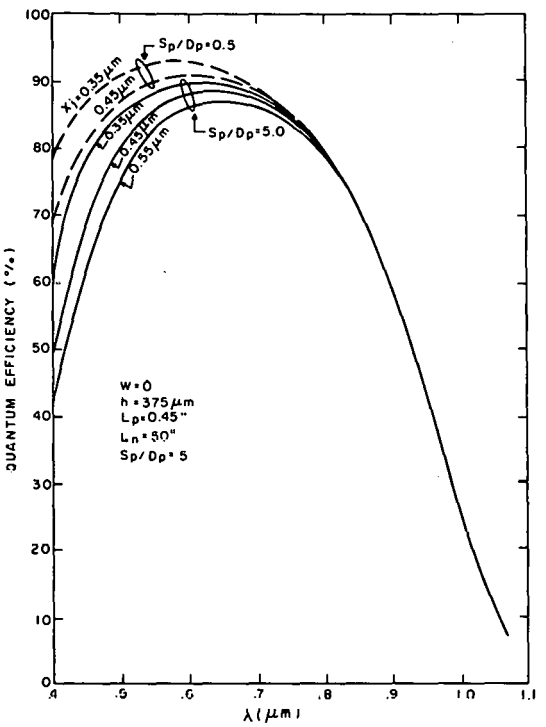

Figure 7. Effect of x_j and S_p/D_p on total quantum efficiency.

lamp. Hence, absolute quantum efficiency can be obtained. The system is checked frequently by measuring a calibrated standard solar cell obtained from NASA (NASA #50 Standard Solar Cell). Their measurement and ours agree to better than 5% over most of the spectral range (10% difference at 1.0 μm).

The measured quantum efficiency curve for single-crystal control cell 405 without AR coating is shown in Fig. 8. This is a diffused-junction cell. The lower curve is the measured quantum efficiency. The upper solid curve is QE_{int}, the internal quantum efficiency. This is obtained by dividing the measured QE by (1-R) where R is the reflectivity of bare polished silicon at the wavelength in question. The reflectivity values have been obtained previously by measurements on similar p-type silicon, and it is assumed in this report that these values hold for all bare silicon, including Wacker polysilicon substrates.

Next, we try to fit this QE_{int} to the simple model for a silicon solar cell discussed in the previous section. The fit obtained and the parameters used for the fit are shown in Fig. 8. We assume a zero surface combination velocity for the back side because of the p^+ diffused region. This assumption will only be important for the control samples where the diffusion length is comparable to the thickness. The actual measured junction depth and cell thickness are used for the fit, which is quite good and yields a minority carrier diffusion length,

L_n = 200 μm. This is typical of good silicon material and accounts for the relatively high efficiency of this cell even though the blue response is not particularly good.

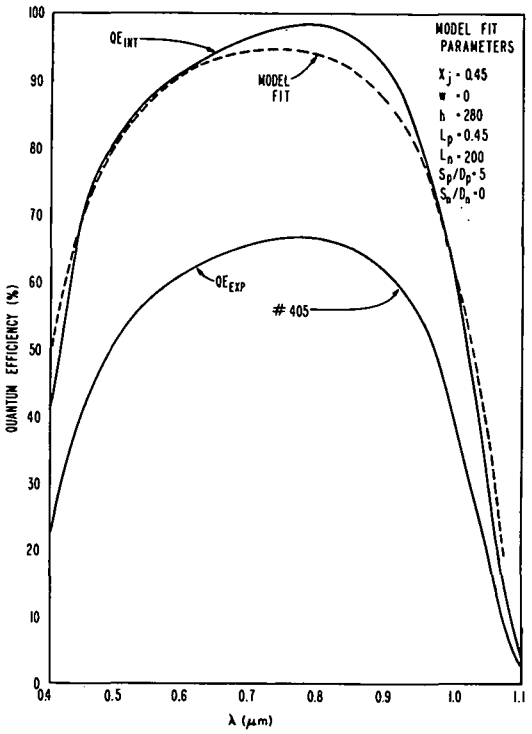

Figure 8. Measured QE curve and model fit for single-crystal control cell 405, diffused junction - cell thickness 0.011 in.

Figure 9 shows the same data for a Wacker polycrystalline diffused-junction cell. The calculated QE_{int} fits the curve derived from the measured QE_{exp} very well. In this case, the minority carrier base diffusion length is only 50 μm. A comparison of Figs. 8 and 9 suggests that the decrease in J_{sc} in the polycrystalline diffused-junction cells is due entirely to this decrease in base diffusion length since the blue response of both cells is nearly identical. This is reasonable; since the diffusion length in the skin region is short even in the single-crystal cell, it is not degraded significantly in the polycrystalline material.

Figure 10 shows the quantum efficiency data for single-crystal control cell 413, which has an ion-implanted junction. Again, the model fit to the

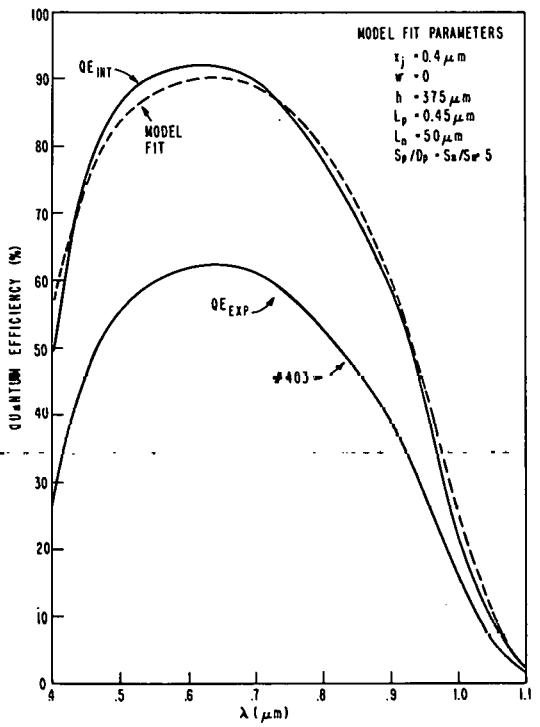

Figure 9. Measured QE curve and model fit for Wacker polycrystalline cell 403, diffused junction - cell thickness 0.015 in.

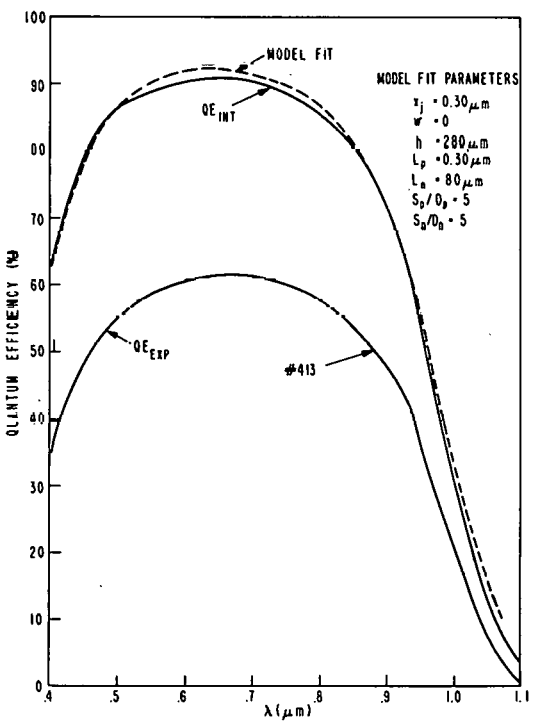

Figure 10. Measured QE curve and model fit for single-crystal control cell 413, ion-implanted junction - cell thickness 0.011 in.

experimental data is very good. In this case, the diffusion length in the base is only 80 μm and this explains the lowered J_{sc} and efficiency of this cell compared to the diffused-junction cell which is made from an identical silicon wafer. Finally, in Fig. 11, we show data for two Wacker polycrystalline cells 414 and 415 which have ion-implanted junctions. The dotted lines are model curves using the base diffusion lengths shown on the curves. Only the QE_{int} curves are shown in Fig. 11. They do not fit the model curves for any choice of L_n, and both curves have very poor photoresponse. For example, cell 415 fits the model curve for L_n = 2 μm for a wavelength up to λ = 0.6 μm. However, for longer wavelengths, the spectral response is anomalously high for such a low diffusion length. It appears that the spectral response of these cells is complicated and cannot be explained by the simple one-dimensional model used for our calculations. In Table 2,

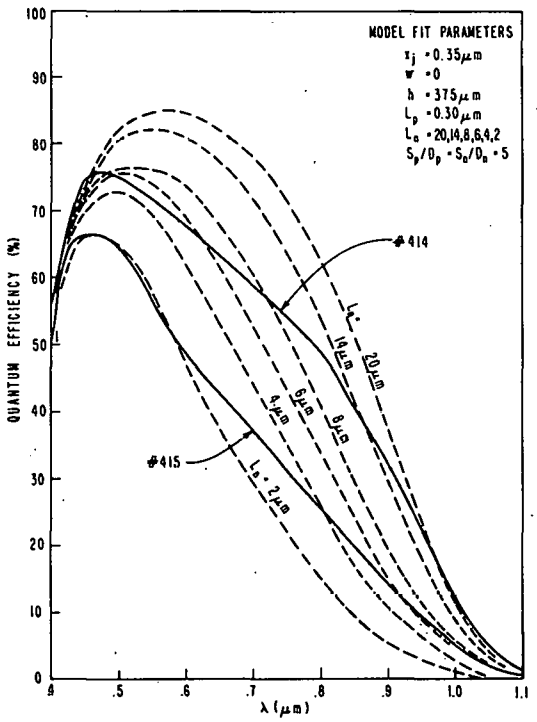

Figure 11. Measured QE_{int} curves for polycrystalline ion-implanted junction cells 414, 415 and model curves for a variety of base diffusion lengths.

the first number listed under the L_n column is the value of L_n which gives the best fit for $\lambda < 0.6$ μm. The number in parentheses is the value of L_n which fits the experimental curve for $\lambda > 0.9$ μm.

3. Measurement of Minority Carrier Lifetime

We have measured the minority carrier lifetime in the base region in a number of Wacker and control solar cells by the diode reverse recovery technique.

In this method, minority carriers are injected into the base region of the diode by a forward current pulse. A pulse of reversed polarity is then applied and the time it takes for the injected carriers to be swept out is measured. This time is simply related to the minority carrier lifetime. The lifetime data can be compared with the diffusion length data obtained from the quantum efficiency (QE) curves by means of the equation $L = \sqrt{D\tau}$ where L is the minority carrier diffusion length; D is the diffusion constant $\sim$ 25 cm^2/s for 6-Ω-cm p-type material, and τ is the minority carrier lifetime.

In Table 9, we list the results for the cells studied. The diffusion lengths as derived from the measured lifetimes are given along with the value derived from the quantum efficiency measurement. The lifetime measurements are carried out on a series of diagnostic dots on either side of the active solar-cell region. These dots vary in diameter from 0.100 to 0.30 in. and are labeled R or L (right or left side of active solar cell), "a" through "d", respectively.

Several observations may be made about these data. For the two control cells, the agreement between the lifetime measurements and the QE measurements is very good. However, for the Wacker cells the lifetime measurements predict a higher diffusion length. For the diffused cell, the measurements predict a

TABLE 9. DIFFUSION LENGTHS IN WACKER AND CONTROL SOLAR CELLS AS MEASURED BY DIODE REVERSE RECOVERY AND QUANTUM EFFICIENCY CURVES

	Meas. Method	Sample Number* 401C	403P	413C	414D	415P
	τ**					
	L a	200	90	85	62	77
(left	b	211	90	85	52	88
side	c	187	71	85	52	50
dots)	d	159	97	--	74	85
	R a	206	75	87	87	81
(right	b	200	72	80	80	57
side	c	151	61	68	68	78
dots)	d	135	63	68	68	79
	QE	250	50	80	6-20	2-8

*Cell 401C - control single crystal, diffused junction
403P - Wacker, polished surface, diffused junction
413C - control single crystal, ion-implanted junction
414D - Wacker, polished surface, ion-implanted junction
415P - Wacker, polished surface, ion-implanted junction
**Lifetime measured by the diode reverse recovery technique.

diffusion length 50% higher on the average than the optically derived diffusion length, whereas for the implanted cells the diffusion length is approximately ten times higher than the quantum efficiency value. In fact, the diffusion lengths are similar for all Wacker cells as well as the ion-implanted control. On the other hand, the QE curves for the Wacker ion-implanted cells were distinctly inferior to the Wacker diffused cells and can not be fit to the single solar-cell model as discussed in Section IV.A.2 of this report. It appears that the minority carrier lifetime measurement is not sensitive to grain boundaries or bulk traps whereas the QE measurement is. It is possible that higher carrier injection levels which may be present in the lifetime measurements could explain this result.

4. Quantum Efficiency Measurements With and Without DC Light Bias

In view of the large minority carrier diffusion lengths calculated from the diode reverse recovery measurements, we decided to measure QE with a dc bias light on the cell. Since the QE measurement uses chopped light (550 Hz), the dc bias should not affect the signal except insofar as it changes the minority carrier lifetime of the chopped-light-generated carriers. This could happen, for example, if the dc-light-generated carriers saturated the traps and recombination sites which normally limit the lifetime of the chopped-light carriers. These recombination sites could be at grain boundaries or in the bulk material.

The experiments were tried for two cells which had greatly different L_n values without dc bias light, namely, cells 403 and 415. The results for cell 403 are shown in Fig. 12. Cell 403 is a diffused-junction cell which had L_n = 50 μm without bias light. As bias light from an ELH lamp was applied with increasing intensity, the QE curve increased and saturated at the level shown in Fig. 12. Although the light intensity was not measured, we believe it was approximately 40% of AM-1 intensity. A model fit to this new curve gives L_n = 70 μm, in good agreement with the minority carrier lifetime measurement.

The effect for cell 415 is even more surprising. This cell had a poor QE to begin with, but it is greatly improved when bias light strikes the cell. In fact for the same light intensity as was used for cell 403, the QE curve obtained is shown in Fig. 13. It is almost identical to cell 403 and also yields L_n = 70 μm, again in agreement with the minority carrier lifetime measurements for that cell. These new values of L_n are actually more consistent with AM-1

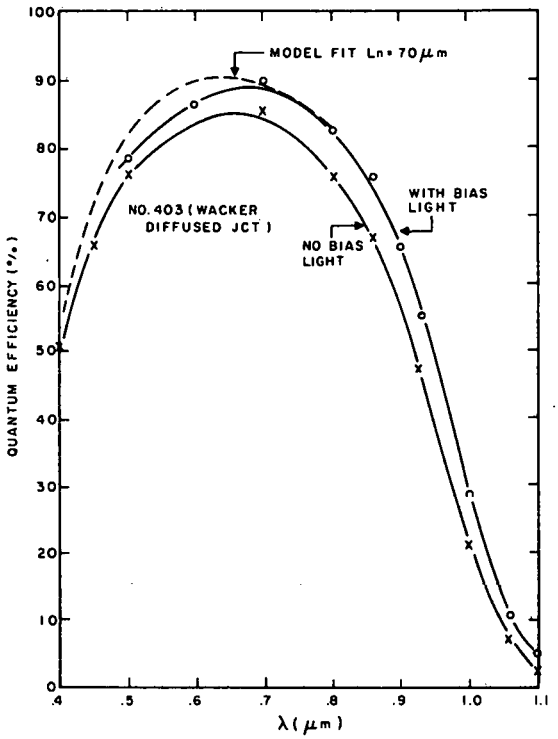

Figure 12. QE curves of solar cell 403 (Wacker, diffused junction) with and without dc bias light.

solar-cell parameters. For example, we find J_{sc} (403) = 19.5 mA/cm^2, J_{sc} (415) = 18.2 mA/cm^2. These two numbers are not too different, in agreement with the light-bias QE curves, but in disagreement with the dark QE curves.

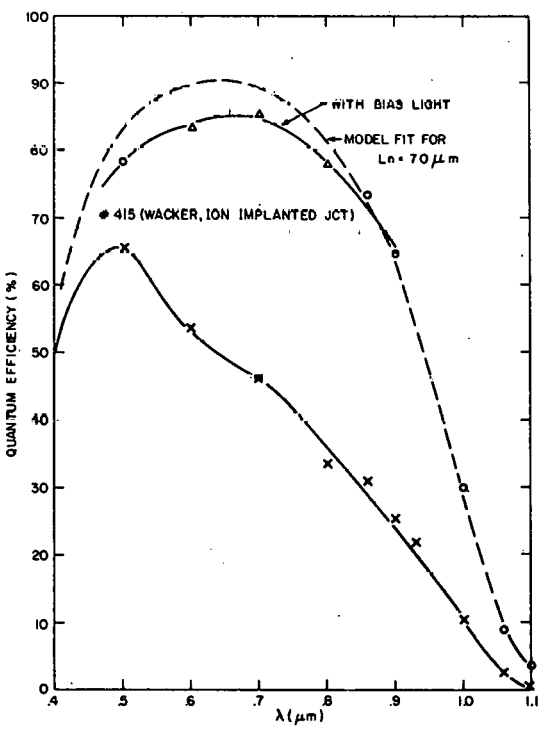

Figure 13. QE curves of solar cell 415 (Wacker, ion-implanted junction) with and without dc bias light.

5. Quantum Efficiency Apparatus With 150-μm-Diameter Light Spot - Single Line Scans

For the proper analysis of grain boundary effects, it would be desirable to measure QE with a very fine spot. Then we could measure QE inside a grain well away from any grain boundaries. Furthermore, if this spot intercepts a grain boundary, the effect of that boundary will be maximized since the total area is small and no illuminated point will be far from the boundary. This is a more difficult problem than with laser scanning, where only one wavelength is required and a laser can be used. It is relatively easy to achieve diffraction-limited optics with the laser, and more difficult with the white light source required for the QE measurement. Nevertheless, we were able to achieve a 150-μm-diameter spot, which appears to be adequate to do the job.

A schematic diagram of the apparatus is shown in Fig. 14. Many of the optical components of our previous QE apparatus are used here. The new feature is the use of two Tropel* collimators. These devices accept a small beam of light (1 to 2 mm) and expand it to a 25-cm beam of collimated light.

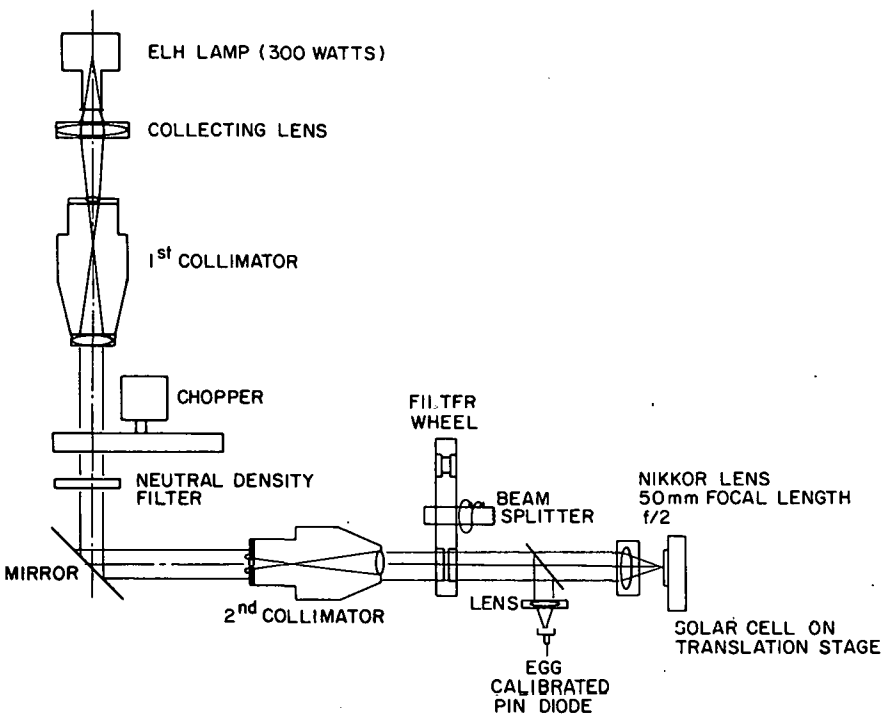

Figure 14. Schematic diagram of the fine light spot (150-μm-diameter) QE apparatus.

*Tropel Co., Fairport, NY.

The second collimator further improves the degree of collimation. The exiting light is parallel to better than 1 degree. The price paid is the loss of most of the light emitted from the lamp. However, sensitivity appears adequate using chopped light and a phase-sensitive detector.

Figure 15 shows a single line scan with the 150-μm light spot across cell 473 (Wacker, diffused junciton). The first trace is taken with unfiltered light from an ELH lamp and therefore has the approximate spectral distribution, but not the intensity of AM-1 sunlight. The sharpness of the metal fingers, which are 85 μm wide, can be used to infer the light spot diameter (~150 μm). A few bumps due to grain boundaries are visible but they are not very pronounced; this is because most of the light is absorbed close to the surface. The second trace was taken over the same line but using filtered (λ = 0.93 μm) light. Now the grain boundary effects are much more pronounced. As the light becomes more penetrating, the grain boundary interaction increases.

This effect can be seen very clearly in Fig. 16. Here we show a single scan in the vicinity of a metal finger, as a function of the wavelength of light used. Note that even at λ = 0.60 μm, close to the normal He-Ne laser wavelength, the grain boundary interaction is still quite small. The magnitude of the interaction increases steadily all the way out to λ = 1.10 μm, the longest wavelength

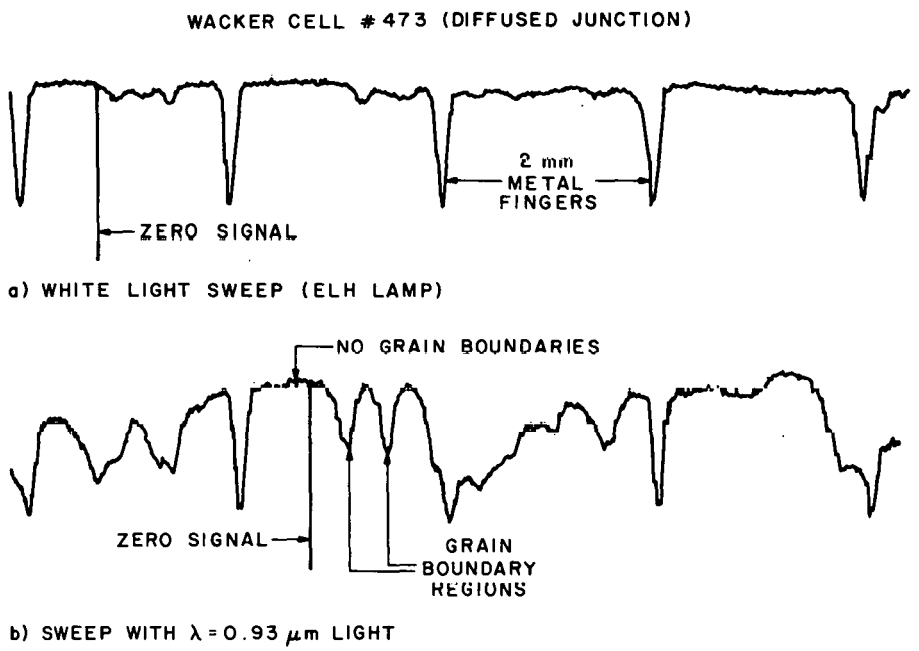

Figure 15. Light scans across Wacker polysilicon solar cell with 150-μm-diameter light spot.

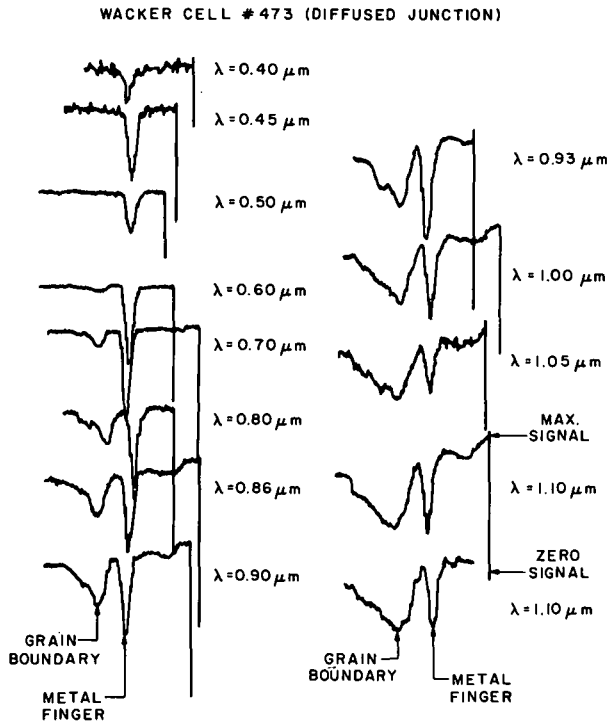

Figure 16. Sweep across a grain boundary and a metal finger for various wavelengths of the 150-μm-diameter light spot.

used. This figure illustrates why $\lambda = 0.633$ μm is a very good choice to obtain laser "maps." That is, the grain boundary "dip" is small and sharp, leading to sharply defined grain boundary lines. On the other hand, if we wish to study the detailed interaction of light-generated carriers with grain boundaries, it is preferable to use longer wavelength light, which enhances the interaction.

6. Quantum Efficiency Measurements - 150-μm-Diameter Light Spot.

Quantum efficiency measurements for an ion-implanted cell are shown in Fig. 17. The top curve is for a single-crystal control (cell 466) which was processed and fabricated at the same time as the Wacker polycrystalline sample (cell 464). For the Wacker cell we show the QE curves for the light spot inside a grain and crossing a grain boundary. We also show an average value obtained by enlarging the light spot to 1.5 cm in diameter so that many grains and grain boundaries are included in the measurement.

The progressive decrease in quantum efficiency in the order shown in the figure is what would be expected. However, we can also obtain quantitative information from the curves. The table included in the figure lists the diffusion lengths obtained from a model fit to the QE curves. In the next column we list

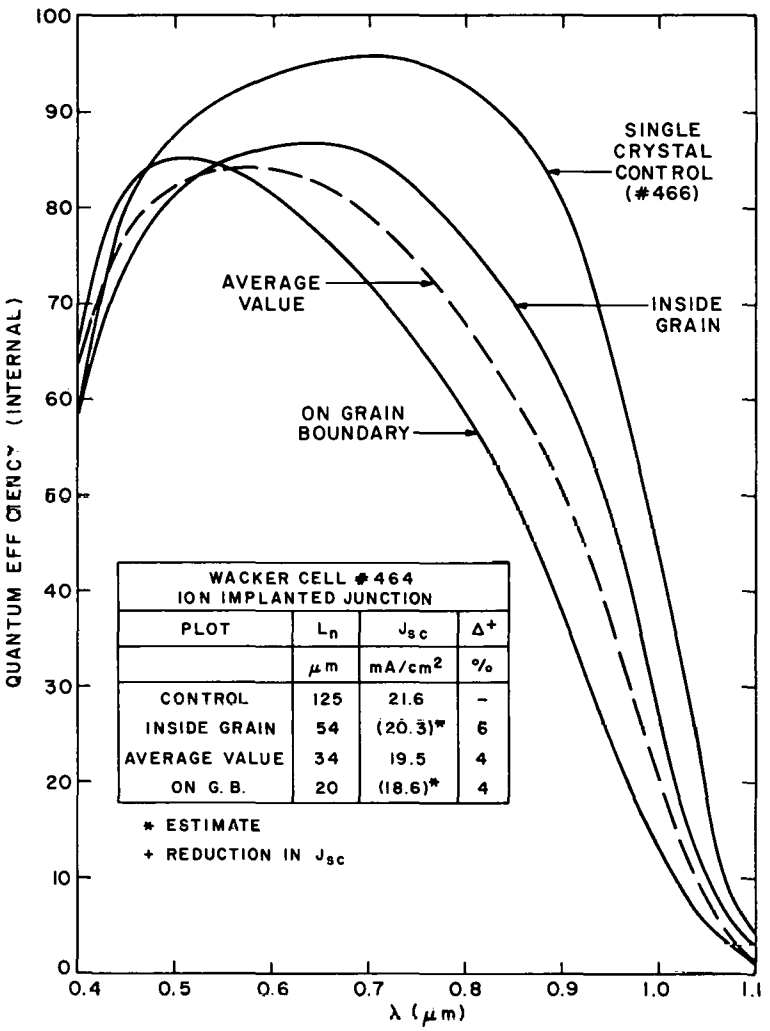

Figure 17. Quantum efficiency curves for an ion-implanted Wacker polycrystalline silicon solar cell.

J_{sc} under AM-1 illumination obtained for the control and the Wacker cell (average value). We then estimate a value for J_{sc}, based on the relative values of the QE curves, for cell 464, inside a grain and on a grain. We do not claim great accuracy for these estimates, but the accuracy should be sufficient for our purpose. J_{sc} (inside grain) is the value we would expect from Wacker polycrystalline material if there were no grain boundaries, while J_{sc} (on grain boundary) is the value we would expect if there were a much higher density of grain boundaries (average grain boundary size approximately 150 μm on a side for our light spot size).

Finally, the last column shows the percent decrease in J_{sc} as we go down the list. For example, a solar cell made from Wacker cast ingot material without any grain boundaries already has a 6% lower J_{sc} than the single-crystal

control. Putting in the actual grain boundary structure reduces J_{sc} by an additional 4%. Finally putting in (conceptually, at least) a larger number of grain boundaries (150-μm average linear dimension) reduces J_{sc} a further 4%. To summarize, analysis of the quantum efficiency curves allows us to separate the effects of bulk properties and grain boundaries on the AM-1 short-circuit current.

Figure 18 shows a similar set of quantum efficiency curves for a diffused-junction polycrystalline solar cell. In this case there is an 8% drop of J_{sc} from the value for the single-crystal control to the estimated inside-the-grain value. The average value shows an additional 7% reduction in J_{sc}. The value of the minority carrier diffusion length inside a grain, i.e., L_n = 75 μm, is similar to other measurements we have made, i.e., the values inferred from minority carrier lifetime measurements and the QE measurements with AM-1 bias applied.

B. LASER SCANNING AND GRAIN BOUNDARY EFFECTS

1. Laser Scans at λ = 0.633 μm

a. Description of Apparatus - Resolution

The original laser scanner we used had a light spot size of 100 μm. Scans taken with this scanner showed irregularities due to grain boundaries, but because of poor resolution, no meaningful maps of grain boundary lines could be obtained. Because the laser scan in this apparatus is obtained by deflecting the beam off a rotating galvanometer mirror, there was no way the laser spot size could be significantly reduced. For this reason, a new scanner was built with much improved optical resolution.

To obtain the small spot size, the laser beam is first expanded and collimated by passing through a commercial laser collimator (Tropel Model 200). Next, the collimated beam is brought to a focus by means of a high quality lens (ultra-micro-Nikkor*, f/2, 55 mm) on the surface of the solar cell under test. Because of the optical arrangement, the solar cell must be mechanically scanned across the stationary focused spot. This is accomplished by means of a micrometer drive run by a smaller motor. The scan made is not yet fully automated, but satisfactory scans can be obtained.

*Nikon, Inc., Garden City, NY.

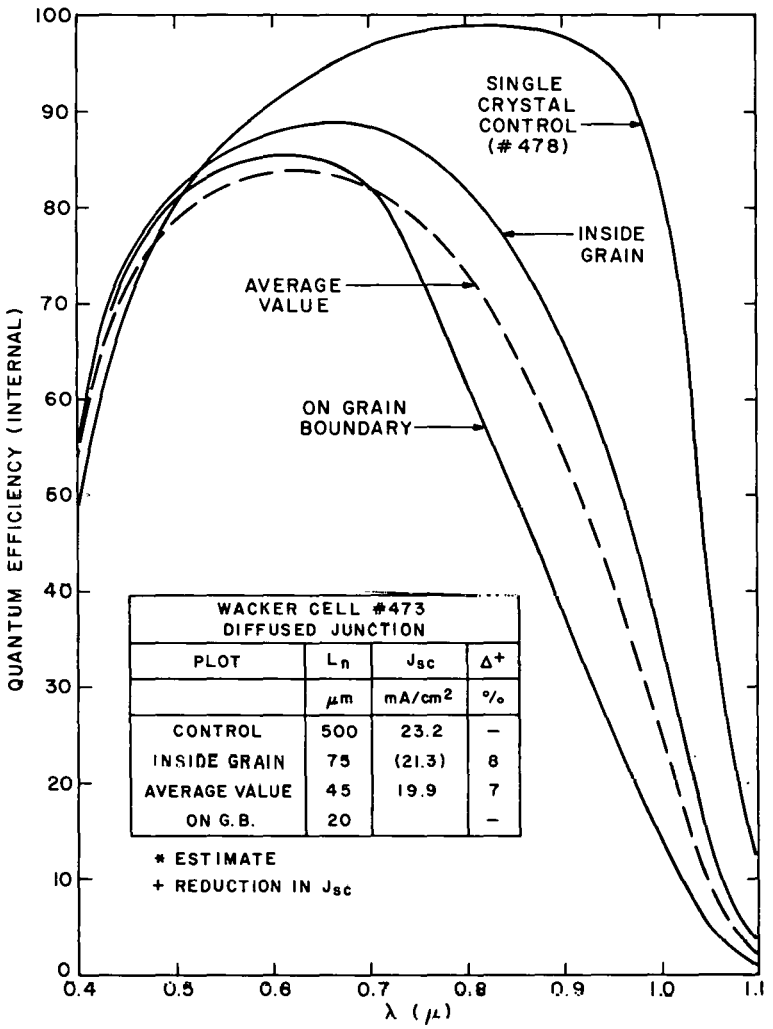

Figure 18. Quantum efficiency curves for a diffused-junction Wacker polycrystalline silicon solar cell.

b. Single Line Scans

Figure 19 shows examples of single line scans. Curve A shows the scan across a single-crystal solar cell. The dips in the curve spaced 2 mm apart are due to the light spot passing over the metal fingers on the top surface of the cell, i.e., there is no photoresponse when the laser spot does not penetrate the silicon. Curve B shows an expanded view of a sweep over a metal finger. This sweep can be used to obtain an upper limit of the laser spot size. The width of the transition region between full photoresponse and zero photoresponse is 6 μm, so the spot size cannot be greater than 6 μm in diameter. Now, the diffraction

limited width of a Gaussian beam at a wavelength of 0.633 μm, focused by an ideal lens, is given by

$$\text{spotsize} = d = 0.8f^{*} \ (\mu m)$$

where f^{*} = f-number = f/d

where f is the focal length of lens = 55 mm and d is the diameter of collimated beam = 10 mm.

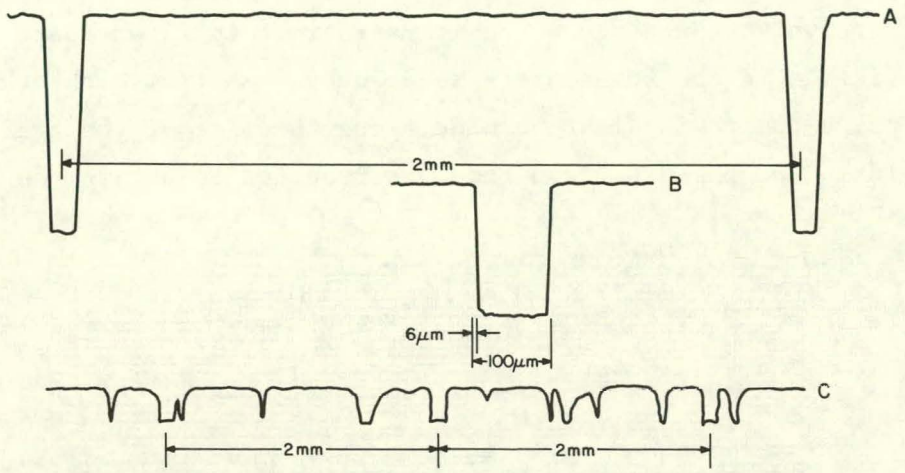

Figure 19. Single sweep laser scan photoresponse curves for silicon solar cells. A. Single-crystal solar cell showing uniform response between two metal fingers. B. Expanded view of metal finger. C. Scan of cell 403, polished surface, diffused-junction, Wacker polycrystalline solar cell, showing metal finger and grain boundary effects.

This predicts a spot size of 4.4 μm which is a little smaller than our experimental upper limit of 6 μm. We thus conclude that our system is behaving properly. We could go to an even smaller spot size by using a larger diameter collimated beam but this might lead to heating and high injection conditions in the silicon solar cell as well as make alignment more difficult. The 4.5-μm spot size appears to be adequate for the task we wish to accomplish. This can be seen in the final sweep C in Fig. 19. This shows a sweep across a section of cell 403, a polished-surface, diffused-junction, Wacker polycrystalline cell. Three metal fingers are visible, spaced 2 mm apart. In this sweep, the full "dip" in photoresponse has been artificially cut off so that the grain boundary signals could be enhanced. All the other dips occur where grain boundaries are crossed. Between grain boundaries, the photoresponse

is quite uniform. We see that some dips are sharp and some are broad. The sharpest dips are about 16 μm wide so that our 4.4-μm spot size is adequate to resolve these effects. In some cases, the broad dips occur because the grain boundary makes an acute angle with the line of the sweep. These effects are more clearly seen where complete sweeps are taken.

c. Laser Scan Maps

Figures 20 and 21 show laser scanned maps of a 5x6-mm^2 area of cells 406 and 414, respectively. Each scan line is approximately 75 μm apart. The four metal fingers visible in the scans are separated by 2 mm from each other. To obtain these maps, a compromise must be made among the size of the grain boundary dip, the resolution of the dips, and the time required to obtain the entire map.

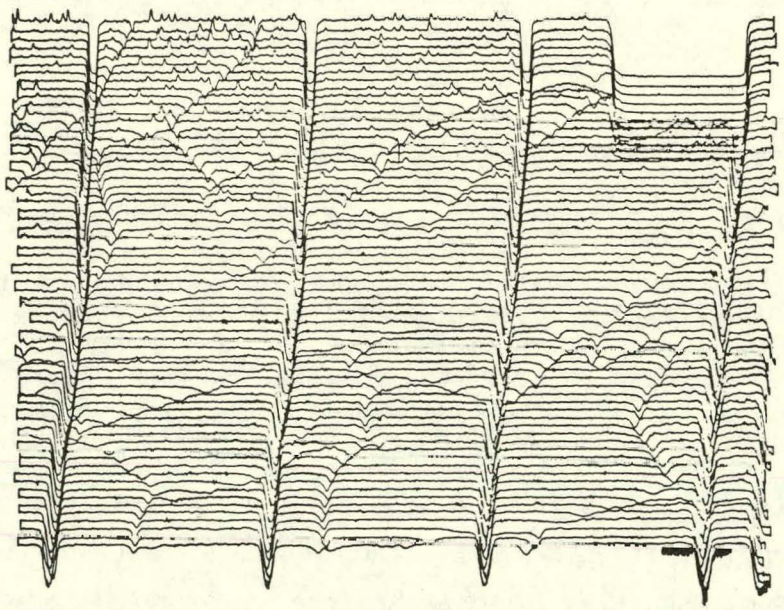

Figure 20. Laser scan of a 5x6-mm^2 area of cell 406, an etched surface, diffused-junction, Wacker polycrystalline solar cell. Spacing between metal fingers is 2 mm.

Therefore, the signals are not as good as can be obtained with a single optimized scan; nevertheless, it is sufficient to show grain boundary lines. Cell 414 which has a polished surface gives a better overall picture. The etched surface of cell 406 produces some surface irregularities which show up in the laser scan. However, Fig. 20 is interesting because we can obtain a photograph showing the grain boundary structure of the same area (Fig. 22). Figure 22 (a) shows the actual photograph, and in Fig. 22 (b) the portion corresponding to the laser

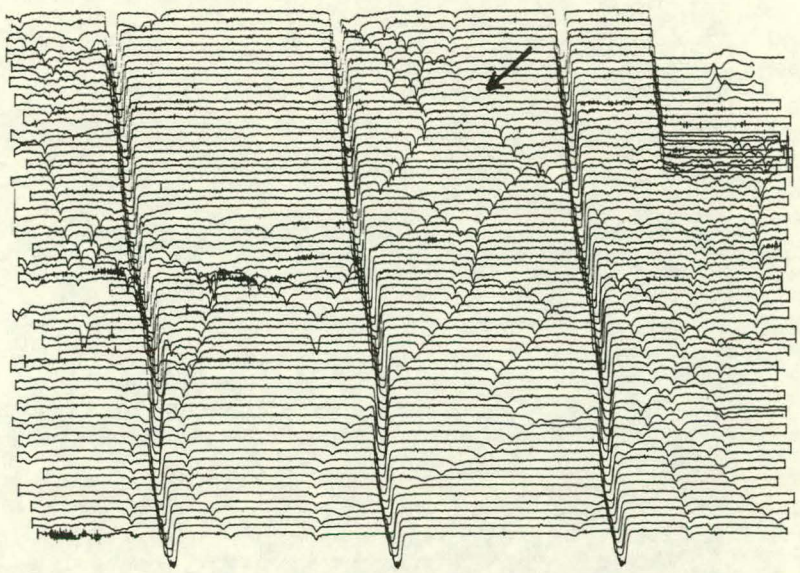

Figure 21. Laser scan of a 5x6-mm^2 area of cell 414, a polished surface, ion-implanted junction, Wacker polycrystalline solar cell. Spacing between metal fingers is 2 mm.

scan of Fig. 20 has been blocked out. The grain boundary lines which can be identified in the laser scan are marked with a heavy line, while the boundaries which do not appear in the laser scan are dotted. Thus, we have the interesting result that some grain boundaries, clearly visible in the photograph, do not appear in the laser scan photoresponse curves. Another interesting feature visible in Fig. 21 occurs along the grain boundary indicated by the arrow. The photoresponse varies along the grain boundary itself, reducing almost to zero near the arrow. This is strong evidence that a grain boundary is not necessarily homogeneous along its length.

2. Laser Scans at λ = 1.15 μm

a. Description of Apparatus

Laser scans at λ = 0.633 μm are ideal for obtaining laser maps of electrically active grain boundary structure. On the other hand, if we wish to study grain boundary photoresponse in detail, then longer wavelength, more penetrating light is preferable. Therefore, we have set up a λ = 1.15 μm laser in our laser scan apparatus.

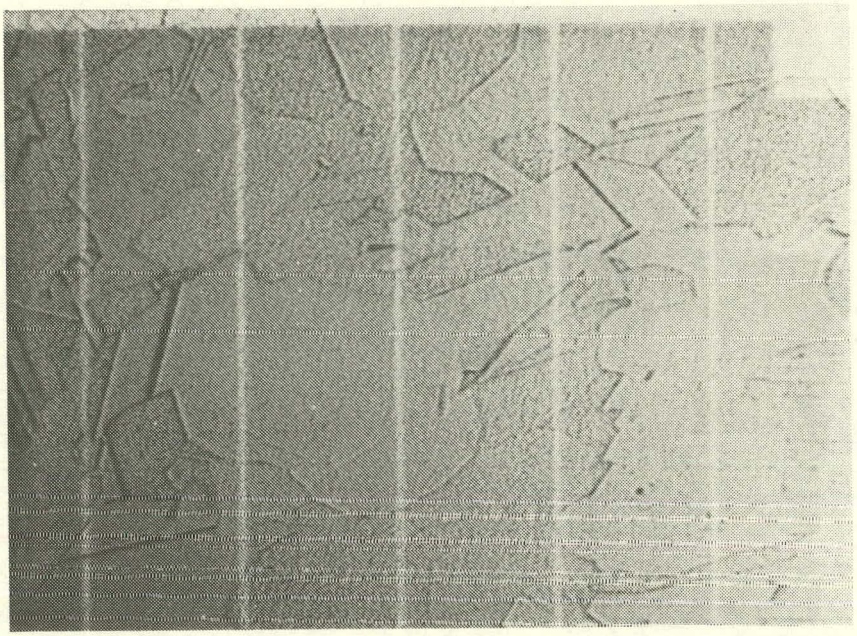

(a)

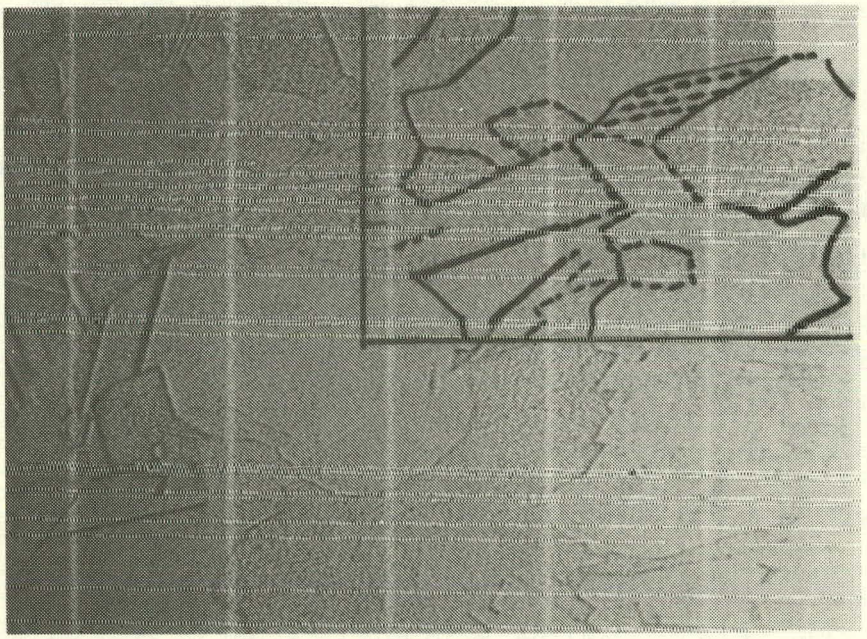

(b)

Figure 22. Photograph of a portion of cell 406. (a) Actual photo. (b) Photo with laser scan area blocked off and laser scan lines marked in heavy lines. Dotted lines are grain boundaries which do not appear in laser scan.

For these experiments a Jodon Engineering Assoc.* Model HN-20B helium neon laser was incorporated into our optical system. This laser emits 20 mW of power at $\lambda = 0.633$ μm or, if the appropriate set of mirrors is used, 5 mW at $\lambda = 1.15$ μm. We are interested in the $\lambda = 1.15$ μm wavelength because light is completely penetrating at that wavelength ($\alpha = 0.5$ cm^{-1}), yet there should be enough absorption to give a reasonable photoresponse signal. With penetrating light we expect the photoresponse dip due to grain boundaries to extend a distance equal to the minority carrier diffusion length on either side of the grain boundary.

We first made some scans with this laser at $\lambda = 0.633$ μm. Then we substituted the long wavelength mirrors and made scans at $\lambda = 1.15$ μm. The results of both measurements are reported below.

b. Line Scans at $\lambda = 0.633$ μm

Figure 23 shows a line scan across cell 464 which has an ion-implanted junction. The sharpness of the metal-finger transitions is used to ensure that the beam is properly collimated and the spot is in sharp focus. With a collimated beam diameter of 2.5 cm, the diameter of the focused spot should be 1.8 μm. Using the sharpness of the metal-finger transition, we find that the spot size is 3.0 μm. This is shown in the expanded scale position of Fig. 23.

The photoresponse looked similar to earlier scans. However, several comments can be made. The full half-width of the narrowest photoresponse observed was 33 μm and the maximum drop in photoresponse was 12%. These are surprising results. Since the penetration of 0.633-μm light in silicon is only 2.8 μm, a dip in photoresponse 16 μm away from the grain boundary cannot be due to diffusion to the grain boundary. Therefore, the bulk diffusion length must be lower near the grain boundary, possibly due to strain or impurity effects associated with the grain boundary.

When the light spot is directly over a grain boundary, we would expect a large drop in photoresponse, since the light spot has such a small diameter (~3 μm). The modest 12% drop may be due to a saturation effect since the intensity of the focused laser spot is much higher than AM-1 illumination. For

*Jodon Engineering Associates, Inc., Ann Arbor, MI.

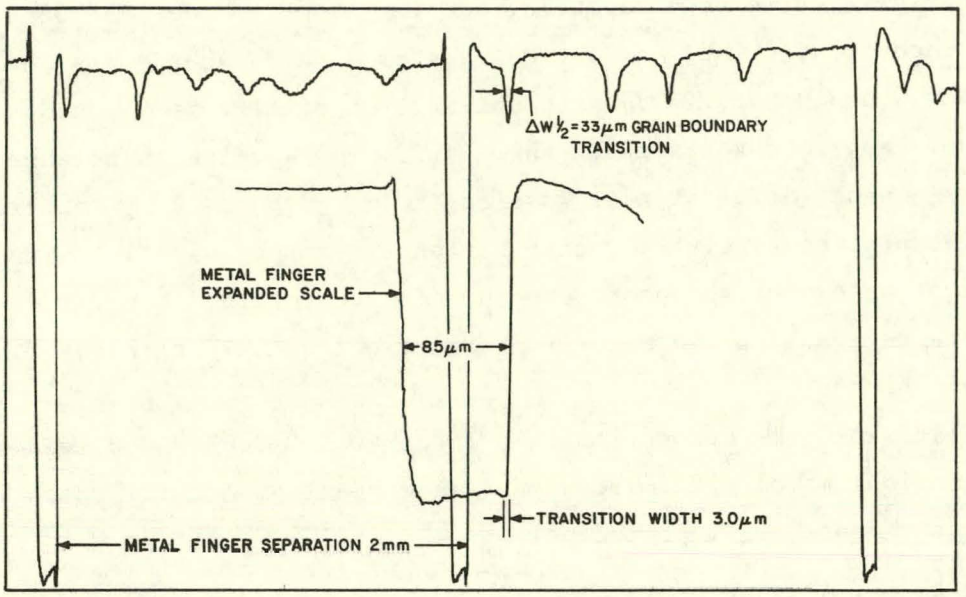

Figure 23. Laser scan (λ = 0.633 μm) showing grain boundary photoresponse dips in cell 464 (Wacker polycrystalline, ion implanted).

example, when the 20-mW laser beam is attenuated by a factor of 100, the current detected in a 100-Ω load resistor is 0.5×10^{-3} mA. If the area illuminated is approximately 8×10^{-8} cm^2, this gives a current density of 5×10^3 mA/cm^2. Under AM-1 illumination, the same cell has J_{sc} = 20 mA/cm^2. Therefore, the current density in the laser spot area is 250 times higher. It may be difficult to reduce the laser power another factor of 200 and still obtain a usable signal.

c. Line Scans at λ = 1.15 μm

The laser scans at λ = 1.15 μm look quite different. The narrowest photoresponse dips have half-widths of 45 to 50 μm. The magnitude of the photoresponse dip is 50 to 75% of the peak signal, i.e., much greater than the photoresponse dip for λ = 0.633 μm light. However, there are many broader lines, up to 300 μm for the full half-width. In fact in the three cells studied (415, 464, 473) the photoresponse is never uniform. This makes it difficult to obtain the exact line shape of the sharp dips, which are needed to obtain quantitative data on the grain boundary recombination velocity.

Laser scans at λ = 1.15 μm for three different solar cells are shown in Fig. 24. The first scan is for a single-crystal solar cell, and shows a uniform

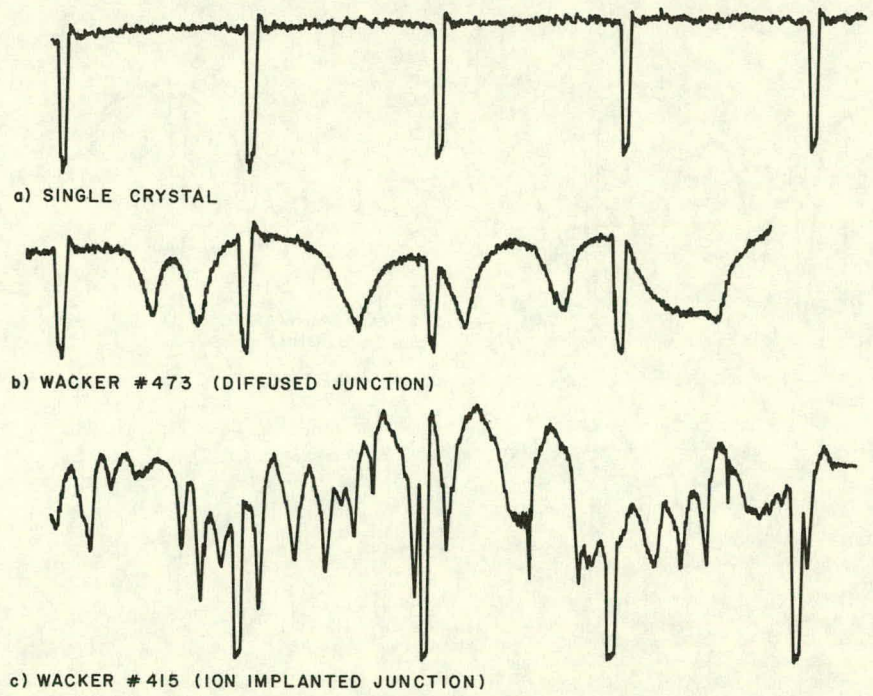

Figure 24. Laser scan (λ = 1.15 μm) of three different solar cells.

response except for the metal finger dips. The second scan is for cell 473 (Wacker, diffused junction). This is a relatively high-efficiency cell and the photoresponse dips are very broad, as we would expect for a high diffusion length material. The third scan is for cell 415 (Wacker, ion implanted), which has a poor efficiency. The grain boundary photoresponse lines are much narrower (by a factor of four), as would be expected for a poor diffusion length material.

In Fig. 25 we compare laser scans for cells 473 (diffused junction) and 464 (ion-implanted junction). If we measure the half-width of the narrowest lines for each scan, we find $\Delta W_{1/2}$ = 280 μm (cell 473), $\Delta W_{1/2}$ = 200 μm (cell 464). Cell 473 has a wider line in agreement with its measured longer base diffusion length (L_n = 75 μm, cell 473 versus L_n = 54 μm, cell 464, see Section IV.A). In fact, interestingly, the ratio of the photoresponse half-widths is almost identical to the ratio of the two diffusion lengths, i.e., 1.40 and 1.39. Naively, one might expect that the photoresponse width (full width, half maximum) would be approximately twice the diffusion length or less. Instead it is almost double that amount. This anomaly cannot be explained at this time.

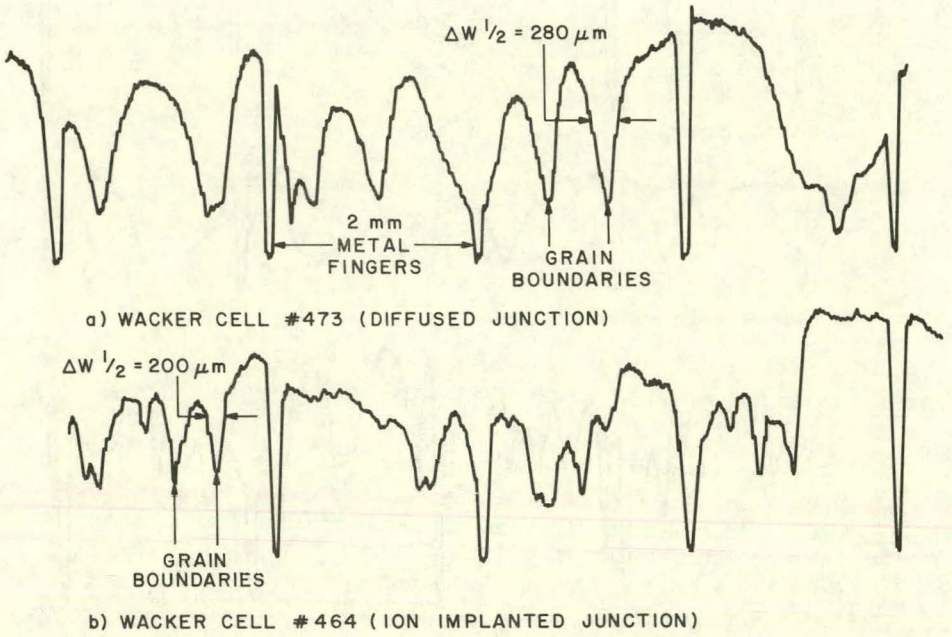

Figure 25. Laser scan (λ = 1.15 μm) of Wacker cell 473 (diffused junction) and cell 464 (ion-implanted junction).

C. DEEP-LEVEL TRANSIENT SPECTROSCOPY (DLTS) IN POLYCRYSTALLINE SILICON

These experiments measure the properties of electrically active "deep" levels that can be associated with the grain boundaries in polycrystalline Si. Such levels are generally believed to be responsible for limiting the performance of solar cells by reducing both I_{sc} (via excess recombination of photocarriers) and V_{oc} (via excess dark generation of minority carriers). The present deep-level transient spectroscopy (DLTS) measurement is capable of detecting very low bulk concentrations ($\sim 10^{11}$ cm^{-3}) of levels which can trap majority carriers, but its use for grain boundary states has not previously been demonstrated. Samples for this purpose consist of small (1 to 2 mm) diodes made photolithographically either as diagnostic adjuncts to the solar cells (i.e., using masks having both cell and "dot" patterns) or as a matrix of dots covering a large area. With the second method applied to Wacker Silso wafers, we have been able to fabricate samples having no visible grain boundaries, one, two, or three boundaries for comparison. Two of these are shown in Fig. 26.

Because the DLTS experiment measures the capacitive properties of a potential barrier region, we have formed p-n junctions in the Wacker material similar

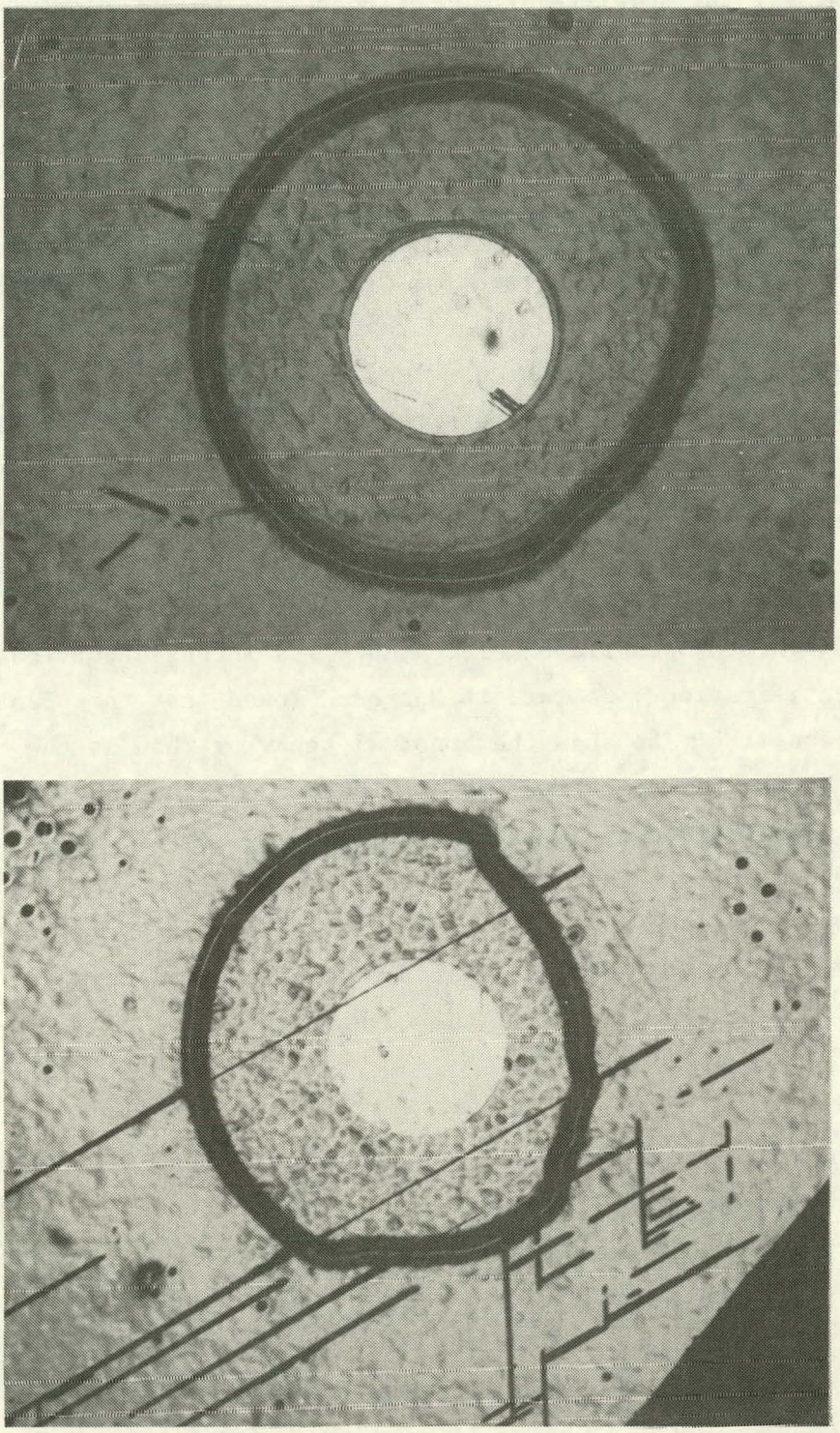

Figure 26. Photographs of diode dots F7 and E7 of wafer 453 (Wacker, diffused junction).

to, or the same as, the solar cells, using both ion implantation and diffusion. The diode sizes are defined by either mesa etching or oxide masking of the added dopant to produce a "planar" device structure in which the junction perimeter is entirely under a good thermally grown oxide. The etched mesas also have a thermally grown oxide on the perimeter. The planar technique, although more tedious in preparation, provides a very different surface condition on the junction perimeter. A control wafer of single-crystal Si accompanied every Silso wafer through the processing sequences.

These measurements have produced evidence that the surface conditions at the junction perimeter may cause DLTS signals that obscure effects in the bulk (i.e., in the volume of the space-charge region of the junction). Under some circumstances, which cannot yet be reliably reproduced, the DLTS curve shows a broad, asymmetrical, negative band rather than the normal type of positive, narrow, usually symmetrical peak. This contrast is illustrated in Fig. 27. The abnormal behavior is thought to be surface-related, but its inconsistency has prevented a definite identification. So far, it has been found that the planar junction structure is less likely to show the abnormal behavior than is the mesa diode. Nevertheless, there are indications that surface contributions may be seen even with the planar diodes.

One other DLTS effect has been observed in some Silso mesa diodes that were exposed to atomic hydrogen to passivate the grain boundaries (see Section V). As shown in Fig. 28, hydrogenation erased one of two broad negative bands in the DLTS curve. Here also, however, the identity of these bands is not yet determined.

The deep-level measurements have to date not succeeded in providing any unambiguous property of electronic states at grain boundaries. To overcome this problem, two avenues are being followed. One is to develop closer control over the device processing to eliminate surface effects. The second avenue is an attempt to fabricate a diode in a Si bicrystal oriented so that the grain boundary is parallel to the junction and close enough that the space-charge region of the junction includes the boundary when reverse bias is applied. This latter structure created very stringent demands on fabrication tolerances; there is no assurance that it can be successfully made.

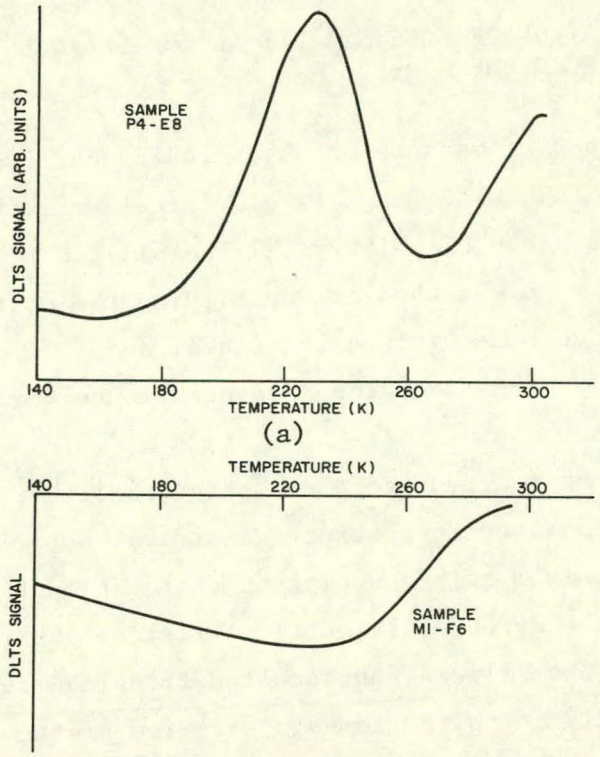

Figure 27. Deep-level spectra (by transient capacitance) of two similar Wacker Silso diodes: (a) a planar structure (Sample P4-E8), (b) a mesa structure (Sample M1-F6).

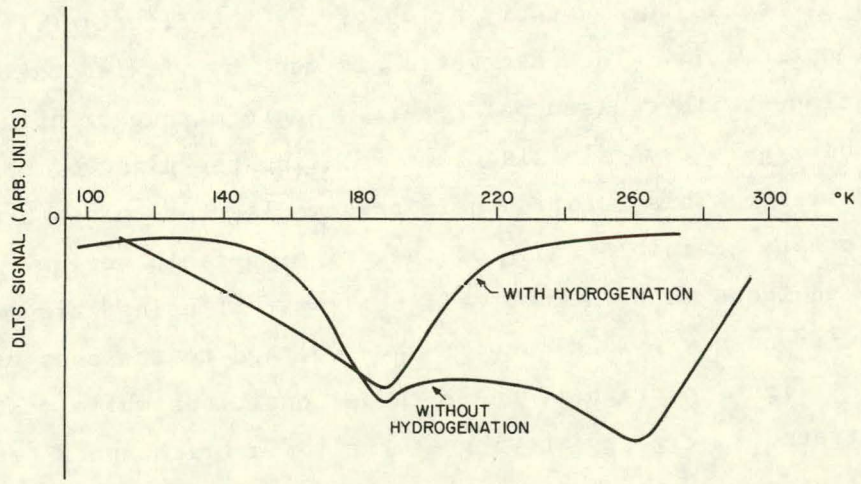

Figure 28. Deep-level spectra (by transient capacitance) of cell 413C (single-crystal control), before and after hydrogenation.

D. SELECTIVE OBSERVATION OF ELECTRICALLY ACTIVE GRAIN BOUNDARIES BY A LIQUID-CRYSTAL TECHNIQUE

A variety of types of measurements, including our own light-spot scans, has shown that there is a wide range of electrical activity among grain boundaries within a single piece of polycrystalline silicon. It would be useful, therefore, to have a simple method of identifying the most active boundaries without having to process a complete solar cell and then perform the detailed scanning measurement. A new technique has been found for this purpose and appears to be quite successful.

This new technique is predicated on the generally established model of grain boundaries which associates strong electrical activity with large potential barriers. It follows from this association that the most active boundaries should also possess the strongest electrical fields. Where a grain boundary meets the surface of the silicon, uncancelled fringing fields can be expected to emerge from the silicon in the immediate region of the boundary. Fringing fields of this sort are utilized in the present technique.

This method uses a thin (~12 μm) layer of liquid crystal to cover the surface of a (generally polished) polycrystalline silicon sample. The optical axis of such liquid crystals is known to be sensitive to electrical fields, and the method here is to sense the boundary by observing the effect of its fringing field on that optic axis. The observation is made by viewing the sample in a microscope equipped with crossed polarizers. Where strong fringing fields exist, they rotate the liquid-crystal axis, thus rotating the plane of polarization of the reflected light. This rotation permits some light to pass through the analyser and create a visible image of the fringing-field region.

It has been found that the most effective way of using this method is by applying a low-frequency (~1 Hz) square-wave voltage to the ends of a sample. Some boundaries light up brightly under these conditions while most stay dark. This is illustrated in Fig. 29 showing at the top a bright path nearly crossing a sample ~8 mm wide. At the bottom is a double exposure of the same region showing the same bright line superimposed on a normal picture of the grain boundaries in that region.

A major advantage of the present method is that the sample being studied needs no processing at all, not even electrical contacts. The effect of the pulsating voltage occurs by capacitive coupling to the sample when it is simply

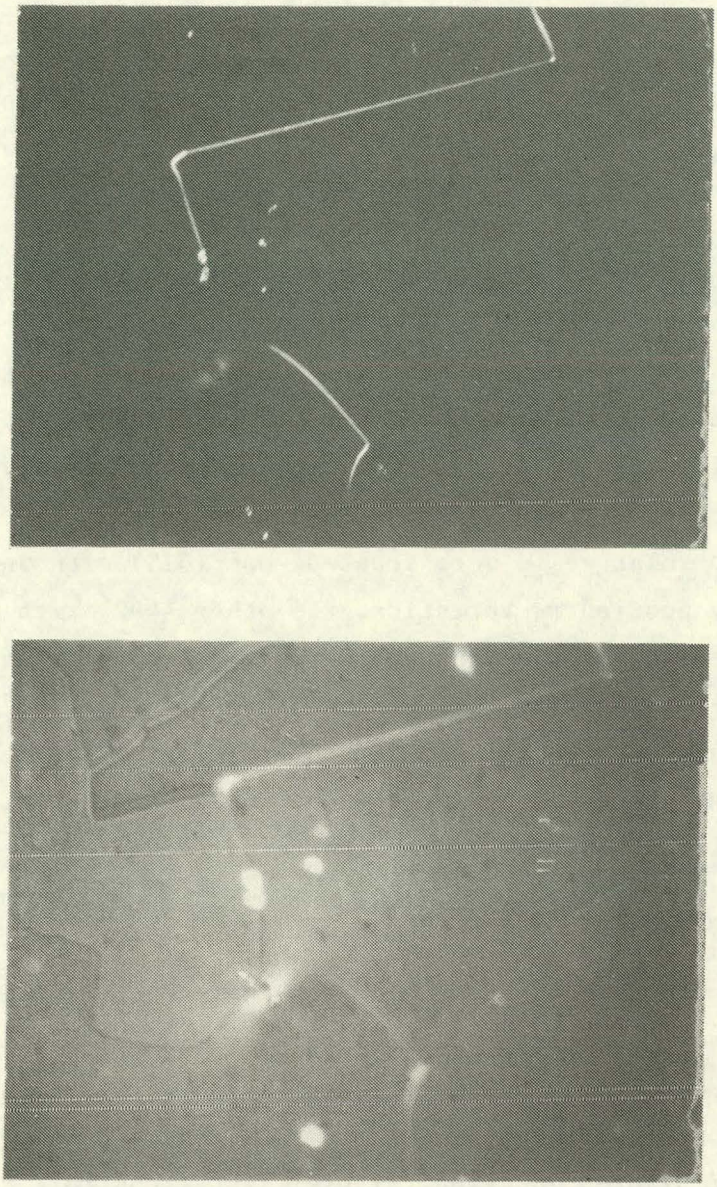

Figure 29. Photographs through a microscope equipped with crossed polarizers of a small area of Wacker polycrystalline silicon with a liquid-crystal film on its surface. Top, active grain boundary lit up; Bottom, double exposure showing other grain boundary structure.

laid onto a pair of metal strips that touch the back of the sample at its ends. This permits the use of any desired direction of the applied voltage, a feature that should permit detailed studies of field-orientation effects. Moreover, the use of capacitive coupling eliminates dc power dissipation in the sample, thus avoiding heat-induced phase change in the liquid crystal.

Correlation of light-spot scan data with this liquid-crystal viewing method is now being undertaken.

SECTION V

PASSIVATION OF GRAIN BOUNDARIES - HYDROGENATION EXPERIMENTS

A. INITIAL EXPERIMENTS ON TWO WACKER SOLAR CELLS

In this section we describe some experiments on the passivation of grain boundaries of completed solar cells fabricated on Wacker polycrystalline substrates by heating them in a glow discharge containing atomic hydrogen. Recently such treatment has been found to greatly reduce the intergrain conductivity of certain polycrystalline silicon samples [2].

This is similar to the treatment which can significantly affect the performance of amorphous silicon solar cells and may lead to the removal of dangling bonds. Two solar cells were treated, one (415) with an ion-implanted junction and very poor characteristics, the other (402) with a diffused junction and good characteristics. The change in solar-cell parameters is listed in Table 10. The I-V curves for cell 415 are shown in Fig. 30. The poorest cell showed the largest improvement, 21% in the efficiency. In a better cell J_{sc} did not change but there was an improvement in V_{oc} and FF. The quantum efficiency of cell 415 was remeasured and found to improve after hydrogenation.

B. MORE DETAILED STUDIES ON FIVE SOLAR CELLS

The initial experiments described above were encouraging. We therefore performed a new series of tests on five solar cells:

401C	Diffused junction, single-crystal control
403	Diffused junction, Wacker
413C	Ion-implanted junction, single-crystal control
414	Ion-implanted junction, Wacker
415	Ion-implanted junction, Wacker

Three different treatments were tried: (1) 300°C, 1 h, in H (plasma discharge); (2) 500°C, 15 min, in He (heat treatment typically used to obtain good ohmic contacts of the Ti-Ag fingers); and (3) 425°C, 8 h, in H (plasma discharge).

The results are shown in Table 11. First consider the two control samples. The ion-implanted sample (413C) shows virtually no change throughout the three

2. C. H. Seager and D. S. Ginley, Appl. Phys. Lett. 34, 337 (1979).

TABLE 10. EFFECT OF HYDROGENATION ON SOLAR-CELL PARAMETERS OF TWO WACKER CELLS

Cell No.	Junction Type	Treatment	J_{sc} (mA/cm^2) before/after	V_{oc} (mV) before/after	FF before/after	η^* (%) before/after
415	Ion implanted	300°C, 1 h in H	17.3/18.9	460/499	0.66/0.68	5.3/6.4
402	Diffused	325°C, 3 h in H	19.8/19.8	535/541	0.71/0.78	7.5/8.3

*No AR coating, AM-1 simulation.

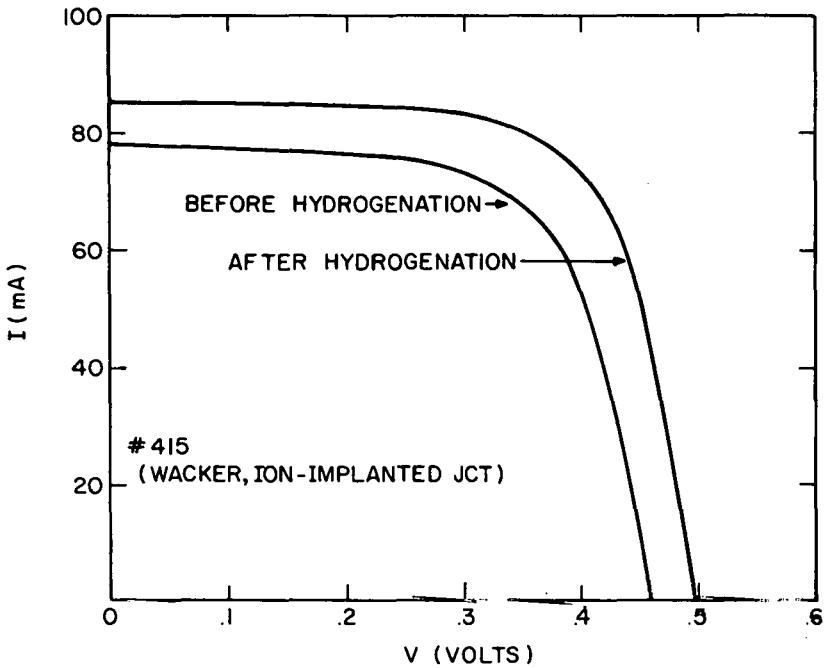

Figure 30. Light I-V curve of solar cell 415 (Wacker, ion-implanted junction) before and after hydrogenation for 1 h at 300°C.

treatments. The diffused-junction cell (401C) shows small variations but the net effect of the three treatments is nil. This is the expected result since these cells have no grain boundaries which can be affected. Next, consider the diffused-junction Wacker cell 403. This shows an improvement of 5% in the efficiency after the first treatment but this is primarily due to an improvement in the fill factor. Only small changes occur after the next two treatments and the net effect is a 3% improvement in efficiency due mainly to the improved fill factor. This improved fill factor is probably just a temperature effect (improved metallization contact resistance) rather than a result of the hydrogenation.

Finally we consider the two Wacker ion-implanted cells. Primarily, these show degradation with each heat treatment except for the first treatment on cell 415, which shows an improvement. This cell had been subjected to two earlier hydrogenation treatments, 300°C for 1 h and 325°C for 3 h. The first of these improved the efficiency by 21%, the second treatment decreased η by 6%, and the first of the present treatments (300°C, 1 h) increased η by 5%. All subsequent treatments decrease η. The final result is that 414 and 415 have decreased in efficiency by 15 and 20%, respectively.

To summarize the results so far, we have obtained one good result, namely, cell 415, which was initially anomalously low in efficiency, was improved by 25%

with a single hydrogenation experiment. On the other Wacker samples, hydrogenation had a small effect or led to degradation of solar-cell parameters. One possible problem is that hydrogenation was carried out on completed metallized cells and some of the metal may diffuse down the grain boundaries during heat treatment.

We plan to perform further hydrogenation experiments in which we will obtain laser scans before and after hydrogenation. This should be a more sensitive measure of the effect of hydrogenation, which may affect only certain very active grain boundaries, than the change in AM-1 parameters. We will also perform hydrogenation on some diodes before they are metallized.

TABLE 11. SUMMARY OF HYDROGENATION EXPERIMENTS ON FIVE WACKER CELLS

	Treatment:	300°C, 1 h in H			500°C, 15 min in He		425°C, 8 h in H		
	Meas. Date:	2/1/79	1/5/79		2/15/79		2/20/79		Total
	Sample No.	Before	After	%Δ	After	%Δ	After	%Δ	%Δ
401C	J_{sc} (mA/cm^2)	22.9	22.2	-3.0	21.9	-1.5	22.6	+3.5	-1.4
	V_{oc} (mV)	562	560	-0.4	560	0	561	+0.2	-0.2
	FF	0.73	0.79	+1.0	0.78	-1.2	0.79	+1.2	+1.2
	η(%)	10.04	9.84	-1.6	9.57	-2.7	10.02	+4.5	0.0
403	J_{sc}	19.7	19.6	-0.5	19.3	-1.5	19.2	-0.5	-2.5
	V_{oc}	530	528	-0.4	530	+0.4	533	+0.5	+0.6
	FF	0.72	0.77	+7.0	0.76	-1.3	0.76	0	+5.6
	η	7.53	7.93	+5.0	7.77	-2.0	7.78	0	+3.3
413C	J_{sc}	19.6	19.6	0	19.6	0	19.6	0	0
	V_{oc}	519	520	0.2	521	0.2	520	0.2	+0.2
	FF	0.76	0.76	0	0.76	0	0.76	0	0
	η	7.73	7.73	0	7.73	0	7.73	0	0.0
414	J_{sc}	19.5	19.2	-1.5	19.5	+1.5	19.4	-0.5	-0.5
	V_{oc}	509	502	-1.4	501	+0.2	471	-6.0	-7.0
	FF	0.70	0.69	-1.4	0.67	-3.0	0.66	-1.5	-5.7
	η	6.93	6.73	-3.0	6.55	-2.7	6.03	-7.9	-15.0
415	J_{sc}	18.9	19.0	+0.5	19.3	+1.5	18.2	-5.5	-4.0
	V_{oc}	483	490	+1.4	492	+0.4	445	-9.5	-10.0
	FF	0.67	0.69	+3.0	0.67	-3.0	0.60	-9.0	-10.0
	η	6.13	6.43	+4.8	6.36	-1.1	4.86	23.6	-20.7

SECTION VI

CHEMICAL AND STRUCTURAL CHARACTERIZATION OF POLYCRYSTALLINE SILICON

A. PHOSPHORUS DIFFUSION PROFILES

In the course of the year, we have established and verified that diffusion depths and diffusion profiles for phosphorus are different, under given experimental conditions, for single and polycrystalline silicon.

For diffusion temperatures between 875 and 925°C (to which we have largely restricted ourselves), diffusion depths measured either by spreading resistance or by staining techniques have systematically been 10 to 20% smaller in Wacker Silso material than in single-crystal material. While these effects are small, they are quite systematic. Secondary ion mass spectrometry (SIMS) has confirmed that this is due to the direct chemical effect of phosphorus, on the average, not diffusing in as far in polycrystalline material. SIMS analyses over areas 200x200 μm^2 have also shown on several occasions that regions of polycrystalline containing grain boundaries exhibit shallower phosphorus penetration than regions in the same specimen well removed from grain boundaries. An example of such a SIMS measurement is shown in Fig. 31. Note that at the spatial resolution of the SIMS analysis, it cannot be ruled out that phosphorus diffuses rapidly down a grain boundary (see below).

The SIMS profiles also indicate that the qualitative shape of the phosphorus distribution differs in single and polycrystalline Si. The distributions, which are far from error function just as with single-crystal silicon, show a more pronounced low concentration "tailing" in single-crystal than in polycrystalline silicon.

In addition to this work, other work (not supported by this contract, and primarily carried out by Ms. Elaine Pope at RCA Laboratories) shows the presence of diffusion spikes extending along grain boundaries beyond the normal junction depth. These observations are obtained from careful beveling and staining experiments and show that about half of the grain boundaries are accompanied by diffusion spikes. Such spikes, although clearly visible, indicate a relatively mild enhancement of diffusion down the boundaries since the length of the spikes appears to be of the same order as the average diffusion length at all temperatures studied.

These results indicate some type of long-range coupling between diffusion down grain boundaries and diffusion far removed from boundaries. The most likely

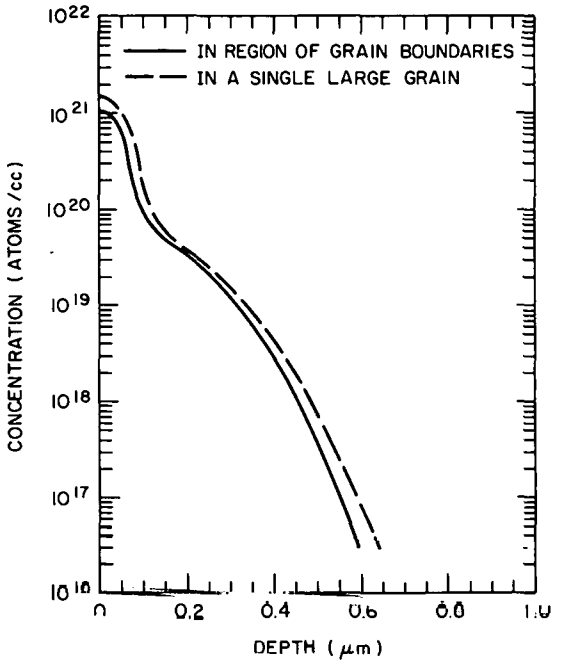

Figure 31. Phosphorus diffusion profile in Wacker polycrystalline silicon.

candidates for such long-range effects are native point defects generated and/or trapped at grain boundaries. In the coming year, we hope to be able, with the help of additional data, to present a qualitative model explaining these results; a quantitative explanation appears very difficult and is perhaps out of the question. It should also be possible, using electron channeling patterns, to study whether grain boundaries exhibiting diffusion "spikes" are crystallographically different than boundaries that do not show these spikes.

B. CRYSTALLOGRAPHIC STUDIES

In order to understand the underlying physical reasons for the different electrical and diffusion behaviors observed, it is clearly necessary to identify, at the very least, the orientation of two grains with respect to each other and to attempt to ascertain what crystallographic planes the boundaries are composed of. The desired results are easy to describe, but not so easy to obtain. After obtaining an optical micrograph and a laser scan to see which boundaries are "active" and which "inactive," we want to be able to identify grain orientations over an entire solar cell, or a substantial fraction of it. Ideally, we want a method which requires no additional preparation of the specimen and, because of the volume of data to be generated on a single cell, which yields the desired data relatively quickly. The well-known methods for determining crystal orientations (Laue diffraction, x-ray topography, or transmission electron microscopy) are undesirable for one or several of the following reasons: absence of an

image corresponding to the diffracting grain, long data acquisition times for a single orientation, long and tedious specimen preparation, or inability to scan over large areas. Of the methods known to us, only electron channeling patterns from selected areas (SA ECPs) seem capable in principle of handling this problem.

Since ECP is a relatively new technique and one which is used relatively infrequently, we present a very brief background to the subject. The interested reader may wish to consult Booker's review [3]. ECPs were first reported 12 years ago by Coates [4]. Under appropriate conditions in the SEM, a set of complex bands can be observed as shown in Fig. 32, which look exactly like Kikuchi bands, familiar from transmission electron microscopy. Like Kikuchi bands, these can be used to determine the crystallographic orientation of the specimen surface with respect to the incident electron beam. Soon after Coates' original observations, techniques were developed for selected areas; here the electron beam is restricted to a small area and the beam is rocked about this fixed area.

The details of the contrast-inducing mechanism are quite complex, but a broad physical understanding can be obtained from the Bloch functions of band theory. The wave function of a high-energy electron (in practice larger than 3 keV) in the crystal can be described as a superposition of two types of Bloch waves: one has maxima along atom planes, the other between atom planes. The actual composition of the electron wave depends on its direction of propagation, therefore depending on the angle between the specimen surface and the incident electron beam. Scattered electrons, primary and secondary, which are observed in SEM preserve a partial "memory" and this results in the SA ECP observed as the beam is rocked.

RCA Laboratories did not have the ability to obtain SA ECPs on our SEM instruments. With the active collaboration of E. R. Levin of RCA Laboratories, we completed the necessary modifications and testing. We estimate that an upper limit for the size of the electron probe is ∿50 μm, which is ample for our purposes. The probe size is probably significantly smaller than this, and we will investigate this further in the future.

3. G. R. Booker, in Modern Diffraction and Imaging Techniques in Material Science, edited by S. Amelinckx, R. Gevers, G. Remaut, and J. Van Landuyt (North-Holland, Amsterdam, 1970) pp. 613-654.
4. D. G. Coates, Philos. Mag. 16, 1179 (1962).

Figure 32 illustrates the type of results we hope to obtain. Figure 32(a) shows a conventional SEM image of an etched sample whose local topography is unusually smooth; a number of grains can clearly be seen. Figures 32(b) and (c) show the SA ECPs of the two points about 200 μm apart indicated as B and C in Fig. 32(a). The ECPs are clearly different, showing that the faint topographic contrast line in the image is indeed a grain boundary.

For our purposes, we found that the surface condition of the specimen was critical to the success of our experiments. We found that polished surfaces yielded excellent ECPs but that there was no topographic contrast at grain boundaries in the SEM. On the other hand, deeply etched surfaces show excellent grain boundary contrast but typically very poor ECPs because of the mottled surface. A successful compromise was found to be a standard polish followed by 15 s of Sirtl etch; satisfactory grain boundary contrast and ECPs in the SEM can be simultaneously obtained. The short etch has the unfortunate feature of removing substantially all of the shallow diffused junction. In future cell fabrication the Sirtl etch will be carried out prior to junction formation. Because of this problem, we have not yet observed ECPs on a solar cell which has been laser scanned. We have, however, studied ECPs on one wafer with excellent results. We obtained orientations of 10 adjacent grains, none of which were in major orientations with respect to the electron beam; most were nearly in {023} orientation; two were nearly in {007} orientation. Adjacent grains of {023} type appeared systematically to be in almost twinned relationship to each other. We expect these results to be typical of Wacker material. We have not yet obtained results on a fully characterized solar-cell assembly, but we see no major impediment to doing so.

We note that we already have strong presumptive evidence that crystallographic orientations are not the only determinants for whether a grain boundary acts as a site for enhanced recombination. This is based on the observation that there are some grain boundaries which, upon laser scanning, show decreased photoresponse along only a portion of their length (see Fig. 21).

C. IMPURITY ANALYSIS

We have verifed through emission spectrography and mass spectrography that the starting Silso materials have purities comparable to standard semiconductor-grade Czochralski silicon. The major impurities present are oxygen and carbon

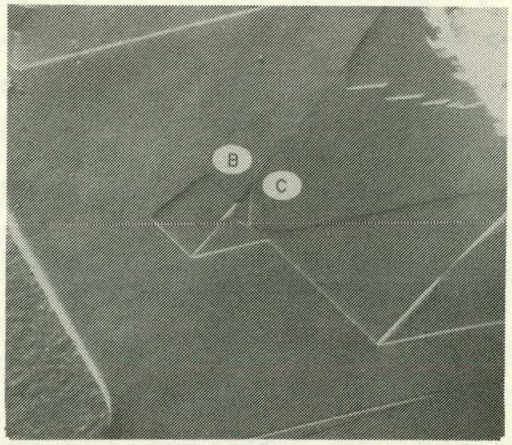

(a)

(b)

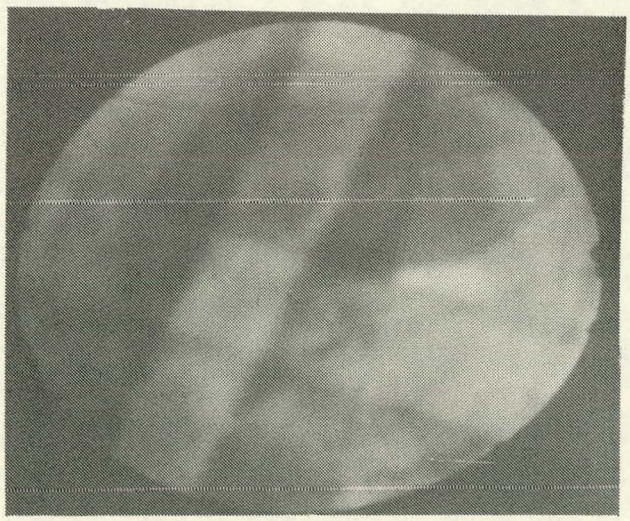

(c)

Figure 32. (a) SEM photograph of Wacker substrate showing regions B and C. (b) Electron channeling patterns taken in region B. (c) Electron channeling patterns taken in region C.

close to their saturation limits. We have occasionally observed second-phase particles, of dimensions approximately 5 μm. Scanning auger analyses of such particles shows only C and Si, implying that they are SiC, probably created during the containment of the silicon melt in a carbon container. Surprisingly, these particles do not seem to affect the characteristics of solar cells, and we therefore have not pursued the matter further.

SECTION VII

GROWTH AND CHARACTERIZATION OF SILICON BICRYSTALS

A. GROWTH OF BICRYSTALS

Two crystal growth runs using bicrystal seeds were made. The seeds were fabricated as shown schematically in Fig. 33. Pairs of standard 1/4-in.-diameter (111) cylindrical seed rods were ground into half-cylinders. The flat surface corresponded to the 110 plane for one half-cylinder and was rotated by angle θ about the (111) axis for the other. The two halves were etched and then wired together to form a seed on which to grow a bicrystal.

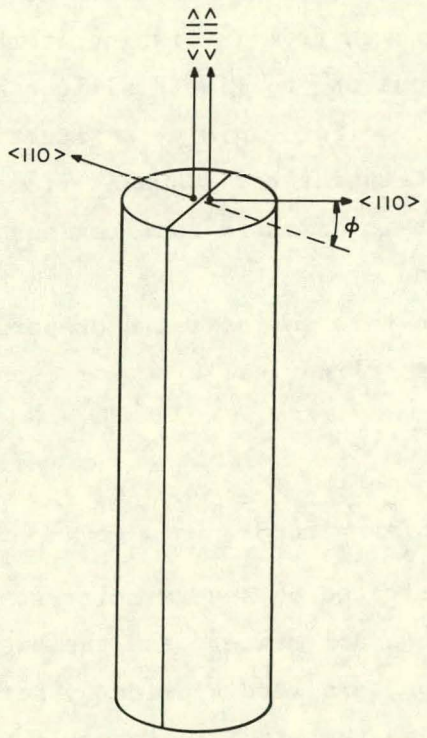

Figure 33. Schematic diagram of growth orientations of silicon bicrystal seeds.

The first growth run was made using a seed pair with $\theta = 30°$. The growth procedure followed conventional practice except that the bicrystal seed was not allowed to melt back at the start of growth, i.e., it was "cold-dipped." During initial seeding attempts at low temperatures, dendrites grew from the boundary between the two seed halves. The dip temperature was raised during successive attempts until dendrite growth was suppressed. The crystal that

was grown is shown in Fig. 34. The intersection of the grain boundary with the surface of the crystal corresponds to a primary growth mode for the grain on the right and a secondary growth mode on the left. The shape of the boundary in the region of the shoulder is shown in Fig. 35. The linear portion of the boundary corresponds to the side of the crystal that is visible in Fig. 34. The other end of the grain boundary terminates in a small cluster of polycrystalline material, probably initiated by the dendrite formation described above. Polycrystalline growth dominated the ingot after about 4 inches of pulling.

The second bicrystal growth run used a seed similar to the first except that $\theta = 5°$. In this experiment we used a high seeding temperature permitting the seed to melt back somewhat. Dendrites were noted here as in the first run, but they melted off spontaneously. In this run it proved to be impossible to prevent polycrystalline growth from initiating at the onset of pulling. We believe that this came about due to liquid silicon being drawn up the space between the two seeds and cooling rapidly, a situation that was avoided in the first run by the low dip temperature. Samples from this second run have not yet been evaluated, and it is possible that regions separated by the desired grain boundary may be found.

A third growth run in this series is in preparation with $\theta = 1/2°$. Additional seed pairs with the cylindrical axis corresponding to (110) are also in preparation.

B. MEASUREMENTS ON BICRYSTAL WAFERS

Solar cells were fabricated on several bicrystal wafers. The junctions were formed by diffusion in the usual manner, and the back surface metallization and the front surface finger pattern were applied by screen printing. The solar-cell pattern was oriented so that the single grain boundary crossed active areas of the solar cell. The AM-1 parameters measured for this cell (no AR coating) are: $J_{sc} = 20.7$ mA/cm^2, $V_{oc} = 568$ mV, FF = 0.72, $\eta = 8.4\%$. The somewhat low fill factor is probably due to the screen-printing technique of applying the metallization.

A laser scan was taken over one of the two small solar cells which were formed on the wafer. This solar cell has dimensions of approximately 6x6 mm^2 and has the grain boundary running through it. This laser scan is shown in Fig. 36. The photoresponse due to the grain boundary can be clearly seen. Figure 37

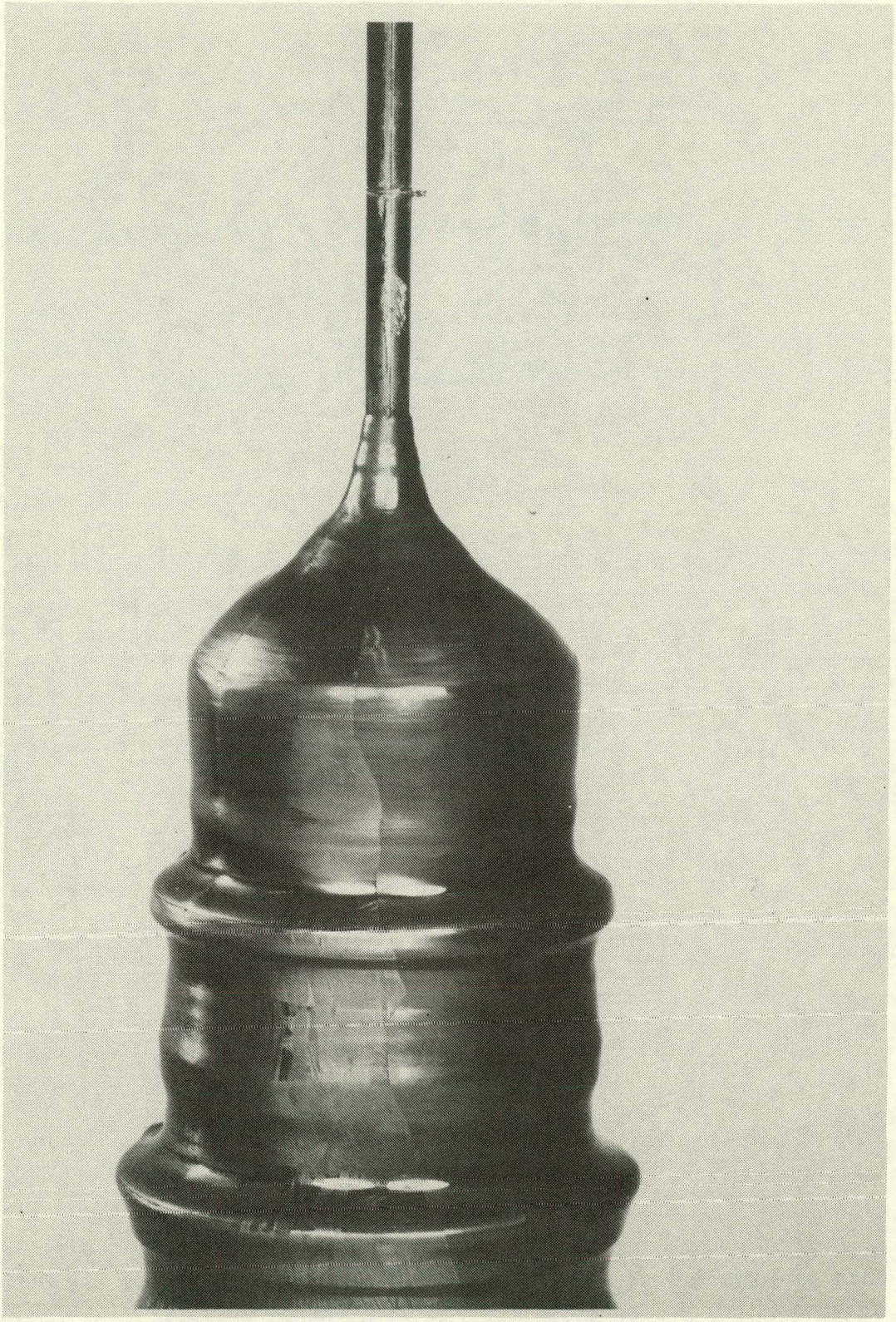

Figure 34. Photograph of a silicon bicrystal with grain boundary visible along the surface of the ingot.

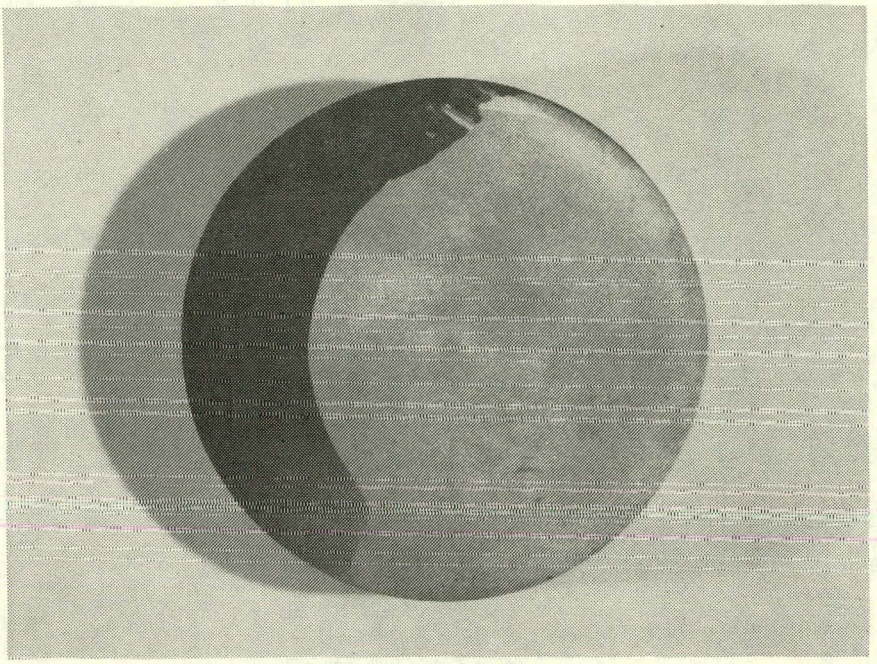

Figure 35. Photograph of a slice out from the silicon bicrystal (30° misorientations) in the region of the shoulder, showing the grain boundary between the two (border between light and dark regions).

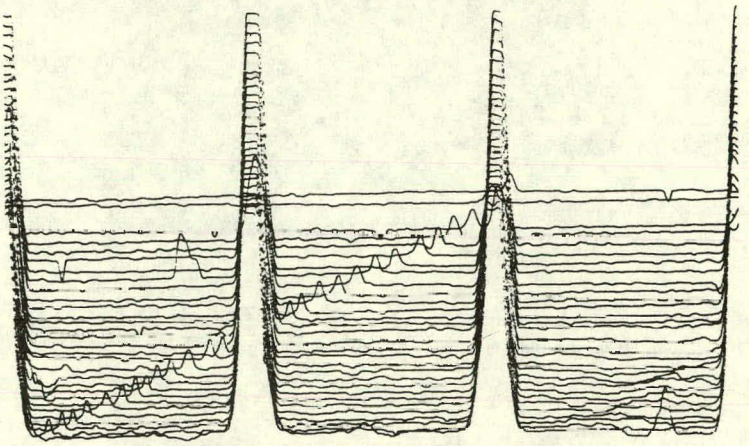

Figure 36. Laser scan of small (6mmx6mm) solar cell showing photoresponse of single grain boundary.

shows an expanded sweep of a single line scan. From it we can determine that the full halfwidth at half maximum of the photoresponse is 44 μm and that the magnitude of the response dip corresponds to an 8.8% drop in the magnitude of the laser-induced short-circuit current.

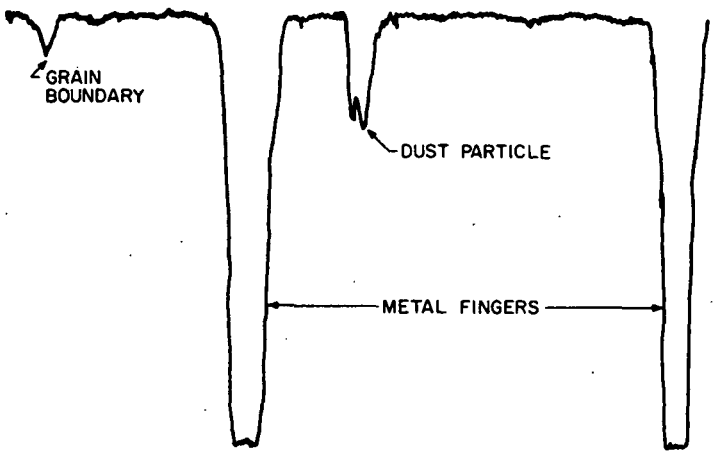

Figure 37. Single laser line scan showing grain boundary photoresponse and two metal fingers spaced 2 mm apart.

SECTION VIII

CONCLUSIONS

The AM-1 efficiency of Wacker Silso polycrystalline solar cells is on the average 20% lower than cells made on semiconductor grade single-crystal wafers, and which receive identical processing. Of this 20%, approximately 12% is directly attributed to grain boundary effects, i.e., an 8% decrease in J_{sc} and a 4% decrease in V_{oc}. This 12% decrease should be reduced as the grain size increases. The remaining 8% decrease is due to the fact that the bulk minority carrier diffusion length is lower in Wacker Silso material than in good Czochralski grown material. This may be due to contaminants introduced by the casting process.

Grain boundary passivation either by atomic hydrogen or phosphorus diffusion down grain boundaries appears to be a promising technique for improving the efficiency of polycrystalline silicon solar cells. However, experiments so far are ambiguous as far as improving cells which already have a fairly high efficiency (e.g., Wacker Silso solar cells). Nevertheless, this approach should be pursued in the coming year.

Several techniques are shown to be effective in analyzing grain boundary effects. These include:

(1) Measurement of quantum efficiency inside and across grain boundaries with a small-diameter (150-μm) light spot.

(2) Laser raster scanning with a $\lambda = 0.633$ μm laser to reveal, by comparison with an optical photograph, which grain boundaries are electrically active.

(3) Laser line scans at $\lambda = 1.15$ μm (penetrating light) to reveal detailed photoresponse near grain boundaries.

(4) Measurement of orientations of individual grains by electron channeling patterns to correlate with grain boundary activity.

(5) Growth of silicon bicrystals with specific misorientations to understand the relationship between misorientation angle and grain boundary activity.

(6) Study of deep traps by DLTS (needs further development).

SECTION IX

PLANNED FUTURE ACTIVITIES

Based on the results of the 1-year investigation reported here, we plan further studies in the following areas:

(1) Correlation between misorientations by electron channeling patterns and grain boundary activity as observed by laser photoresponse.

(2) Continuation of bicrystal studies.

(3) Grain boundary passivation by

  (a) Phosphorus diffusion - study effects of diffusion temperature and presence of phosphorus diffusion "spikes" down grain boundaries.

  (b) Atomic hydrogen - study grain boundary laser photoresponse of active grain boundaries before and after hydrogenation, as well as its effect on AM-1 parameters.

(4) Develop DLTS technique, especially by use of a bicrystal grain boundary parallel to the junction.

(5) Extend work to other forms of low-cost polycrystalline silicon, e.g., ribbon, silicon-on-ceramic, and epitaxial films grown on upgraded metallurgical grade silicon.

REFERENCES

1. H. J. Hovel, in Semiconductors and Semimetals, Vol. 11, R. K. Willardson and A. C. Beer, eds. (Academic Press, New York, 1975), ch. 2, "Solar Cells."
2. C. H. Seager and D. S. Ginley, Appl. Phys. Lett. 34, 337 (1979).
3. G. R. Booker, in Modern Diffraction and Imaging Techniques in Material Science, edited by S. Amelinckx, R. Gevers, G. Remaut, and J. Van Landuyt (North-Holland, Amsterdam, 1970) pp. 613-654.
4. D. G. Coates, Philos. Mag. 16, 1179 (1962).

REPORTS AND PRESENTATIONS

In addition to this Final Report, the following reports were prepared and submitted under this contract:

B. W. Faughnan, Thin-Film Polycrystalline Silicon Solar Cells, SAN-1876-1 Quarterly Report No. 1, prepared under Contract No. ET-78-C-03-1876, January 1979.

B. W. Faughnan, Thin-Film Polycrystalline Silicon Solar Cells, SAN-1876-2, Quarterly Report No. 2, prepared under Contract No. ET-78-C-03-1876, May 1979.

B. W. Faughnan, Thin-Film Polycrystalline Silicon Solar Cells, SAN-1876-3, Quarterly Report No. 3, prepared under Contract No. ET-78-C-03-1876, July 1979.

The following presentation was made:

"Grain Boundary Effects in Polycrystalline Silicon Solar Cells," by Brian W. Faughnan of RCA Laboratories at the 21st Electronic Materials Conference, University of Colorado at Boulder, July 27-29, 1979.

☆U.S. GOVERNMENT PRINTING OFFICE: 1980—640-258/2205